Band Alignments, Band Gap, Core-levels and Valence-Band States in Cu_3BiS_3 for Photovoltaics

Thomas J. Whittles,[†] Tim D. Veal,[†] Christopher N. Savory,[‡,∥] Peter J. Yates,[†] Philip A. E. Murgatroyd,[†] James T. Gibbon,[†] Max Birkett,[†] Richard J. Potter,[¶] Jonathan D. Major,[†] Ken Durose,[†] David O. Scanlon,[‡,§,∥] and Vinod R. Dhanak[*,†]

†*Department of Physics and Stephenson Institute for Renewable Energy, University of Liverpool, Liverpool, L69 7ZF, United Kingdom*

‡*Department of Chemistry, University College London, Christopher Ingold Building, London WC1H 0AJ, United Kingdom*

¶*Department of Mechanical, Materials and Aerospace Engineering, School of Engineering, University of Liverpool, Liverpool, L69 3GH, United Kingdom*

§*Diamond Light Source Ltd., Diamond House, Harwell Science and Innovation Campus, Didcot, Oxfordshire OX11 0DE, United Kingdom*

∥*Thomas Young Centre, University College London, Gower Street, London WC1E 6BT, United Kingdom*

E-mail: Vin@liverpool.ac.uk

Abstract

The earth-abundant semiconductor Cu_3BiS_3 (CBS) offers promising photovoltaic properties, and is often considered analogous to solar absorbers copper indium gallium diselenide (CIGS) and copper zinc tin sulphide (CZTS) despite few device reports. The extent to which this is justifiable is explored via a thorough x-ray photoemission spectroscopy (XPS) analysis: spanning core levels, ionisation potential, work function, surface contamination, cleaning, band alignment, and valence band density of states. The XPS analysis overcomes addresses the shortcomings of prior XPS studies of this material. Temperature-dependent absorption spectra determine a 1.2 eV direct band gap at room temperature; the widely reported 1.4–1.5 eV band gap is attributed to weak transitions from the low density of states of the topmost valence band previously being undetected. Density functional theory HSE06+SoC calculations determine band structure, optical transitions, and well-fitted absorption and Raman spectra. Valence band XPS spectra and model calculations find the CBS bonding to be *superficially* similar to CIGS and CZTS, but the Bi^{3+} cation (and formally occupied Bi-6s orbital) have fundamental impacts: giving a low ionisation potential (4.98 eV), suggesting that the CdS window layer favoured for CIGS and CZTS gives detrimental band alignment, and should be rejected in favour of a better aligned material in order for CBS devices to progress.

Keywords

XPS, photoemission, band gap, ionization potential, Cu_3BiS_3, density functional theory

1 Introduction

Given the plethora of materials vying for research interest in the solar photovoltaic (PV) community, earth abundance is arguably one of the more critical factors to consider when investigating novel materials for use as solar absorbers, so that commercial viability can, in

the future, be a realistic possibility.[1–3] As such, research has shifted away from the established thin film solar absorbers cadmium telluride (CdTe) and copper indium gallium diselenide (CIGS) because of the toxicity or scarcity of the constituent elements. Copper zinc tin sulphide/selenide (CZTS) has shown promise to overcome these factors, however, the five-element makeup of this material makes reliable production a challenge,[4,5] and increases the likelihood of problems associated with defects[6] and secondary phases.[7] The ternary copper chalcogenides with the form $Cu_nM_mCh_x$ (M = Sb, Bi; Ch = S, Se), are an attractive for use in PV because they fulfill the above criteria whilst also having electronic structures superficially similar to CIGS, replacing trivalent In and Ga with Sb or Bi.[8] Ternary Cu-Sb- and Cu-Bi-chalcogenides and the broader class of materials containing post-transition metal cations with an ns^2 electronic configuration (that is, an N-2 oxidation state) have recently been comprehensively reviewed in terms of their solar absorber credentials.[9,10]

Given these aspects, the compound Cu_3BiS_3 (CBS) is attractive because Bi has greater world reserves and ore extraction rates than In, and is therefore much cheaper.[11] While CBS has been known as the mineral wittichenite since 1805[12,13] and was artificially grown as early 1947,[14] its potential for solar PV was not recognized until 1997.[15] Promising PV properties reported include: inherently p-type conductivity;[8] a $\sim$1.4 eV band gap;[16–20] and strong absorption,[17,19,21] calculated to be greater than not only CIGS but also CZTS.[22] Despite these promising early findings, investigation of CBS for application as PV absorber has been sporadic.[23–26] Very few device results have yet been reported, with the best power conversion efficiency only 1.28%.[27] However, the significant PV potential of this material continues to generate interest.[28]

Two key issues to address for any fledgling solar PV absorber are developing reproducible growth of phase-pure material, and establishing the full nuances of the electronic structure. Rigorous characterization of single-phase material, together with detailed electronic structure understanding will allow device structure design for the optimal use of CBS.

A related group of PV-relevant materials with stoichiometry $CuMCh_2$ was developed

in order to find earth-abundant element replacements for the scarce elements in CIGS, indium and gallium.[9,29,30] In contrast to this, CBS seems to have been pursued independently, developing from attempts to synthesize the natural mineral wittichenite.[15,24,31] The subsequent discovery that CBS has PV-relevant properties[21] led to comparisons with the $CuMCh_2$ family. The research which followed saw it likened to CIGS[16,31,32] from a growth perspective,[17,23,33] and in terms of cell architecture,[25,26,34] as done previously with $CuSbS_2$ (CAS).[35] It is not yet clear whether drawing analogies with CIGS is helpful or not, in the way that has previously been applied to the related materials of CZTS[4] and CAS.[36] In spite of the Bi in CBS being trivalent like the In and Ga in CIGS, CBS deviates from the usual tetrahedral structure of the absorber materials derived from silicon.[22,37] Instead it has a different stoichometry and the lattice is distorted with respect to regular tetrahedra.

The crystal structure of CBS is orthorhombic, space group number 19, $P2_12_12_1$. The structure is illustrated in Figure 1 and shows the complex and distorted nature of the structure with respect to the close-to-regular tetrahedra present in CIGS.[37] CBS has distorted tetrahedral BiS_3 units with the Bi atoms three-fold coordinated to sulphur and with the Bi atom at one vertex of the tetrahedron. This resembles the single coordination environment seen in bismuthinite Bi_2S_3, where this type of polyhedron makes up the ribbon ends.[38,39] These are derived from regular octahedra; the lone pair on the Bi replaces a sulphur atom at a vertex of the octahedron, generating distorted square-based pyramids[16] (the other coordination environment in Bi_2S_3,[38]) and then the displacement of the Bi atom due to the presence of copper which stretches the two Bi-S bonds so they are no longer considered.[8,13] While the Cu atoms also have three-fold coordination to S, they instead form near-planar distorted trigonal CuS_3 units which are highly-irregular tetrahedra; low chalcocite Cu_2S also has these polyhedra.[40] These individual structural motifs are depicted separately in Figure 1b. This structure of CBS, consisting of a combination of Cu_2S and Bi_2S_3, is not unexpected as CBS was first made by dry fusing these two materials together.[14] Although both copper and sulphur have three different lattice sites, their coordination is unchanged and

only bond lengths and angles differ by a slight degree and these are labelled in Figure 1a. A more detailed description of the structure of CBS is available elsewhere.[13,22] A greater understanding of the role of the peculiarities of this structure in determining its properties will permit further development of applications of this material.

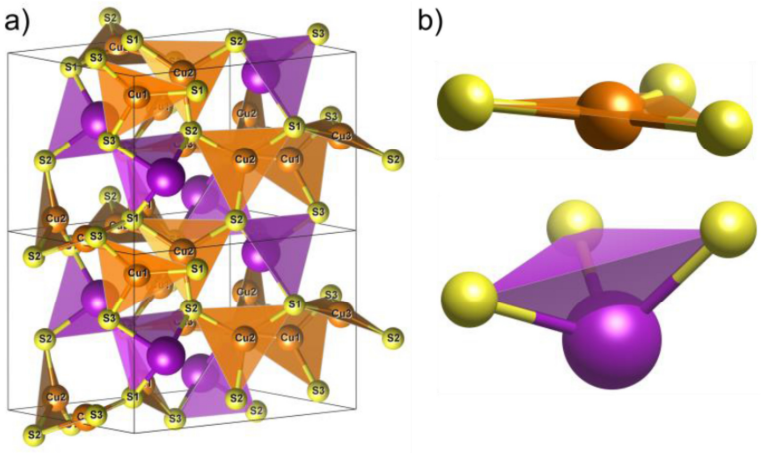

Figure 1: a) Crystal structure of wittichenite[13] CBS. The Cu, Bi and S atoms are shown in orange, purple and yellow, respectively. The numbers denote the inequivalent Cu and S sites in the structure. b) The BiS_3 and CuS_3 structural units.

In this article, a full XPS analysis of CBS is presented. This includes core-levels before and after in situ surface preparation, natural band alignments, and valence band spectra. The CBS films are established as being single phase using x-ray diffraction, XPS and Raman data. Optical absorption between 80 and 320 K is used along with band structure calculations to determine the band gap. The XPS data is corroborated with theoretical density of states calculations which ultimately enable the nature of the bonding in CBS to be related to the band structure and band alignments and therefore allow the optimal solar cell architecture to be determined. Similarities and important differences between CBS and other common solar absorbers are discussed; commonly drawn analogies between CBS and common solar absorbers are found to be limited and unhelpful for the future development of CBS as a PV

absorber.

2 Methods

2.1 Experimental methods

Films of Cu_3BiS_3 were formed by sulfurizing Cu-Bi metallic 'precursor' films. The metal films were thermally evaporated onto plain soda lime glass from 99.999% Cu shot (Alfa Aesar) and 99.99% Bi pellets (Advent Research Materials) to a total thickness of 500 nm. The ratio of thicknesses used was 1:1, since this corresponds accurately to a 3:1 Cu:Bi atomic ratio. Sulfurisation was performed by enclosing the precursor films in a graphite box with 500 mg of elemental sulfur under a 300 Torr atmosphere of dry nitrogen at 375°C for 30 mins. This generated continuous brown/black films with good adhesion that were confirmed to be Cu_3BiS_3 by θ - 2θ XRD as shown in the results section. A wide range of Cu:Bi composition ratios and sulfurization temperatures were trialled. The 3:1 ratio and 375°C were selected since: a) the extremes of composition gave unwanted phases - Cu-rich giving Cu_2S, and Bi-rich giving Bi_2S_3, elemental Cu and a small amount of $CuBiS_2$ in addition to the target phase, and b) the use of temperatures greater than 375°C gave increasingly narrow ranges of tolerance to composition variation in the precursor for the formation of phase-pure Cu_3BiS_3. High temperatures also encouraged poor adhesion and film loss.

X-ray diffraction was performed using a Philips X'Pert diffractometer (PW3050/65 goniometer) in Bragg-Brentano geometry with Cu $K_{\alpha 1}$ (0.15406 nm) x-rays incident from a 4-crystal Ge(220) monochromator, shaped by divergence, progressive receiving (PRS), and anti-scatter (PASS) slits. Scans studied from 10 to 80 degree 2θ with 0.01 degree 2θ step and 1 second dwell time per step.

Raman spectra were measured with a Horiba Scientific Jobin-Yvon LabRam HR confocal Raman microscope. Backscattering geometry was used with an incident wavelength of 514.5 nm from an argon ion laser with a CCD exposure time of 30 s and five acquisitions.

The spectrometer was calibrated to the zero order and the 520 cm^{-1} Raman line of silicon.

Transmission and specular reflection spectroscopy was performed at 11° angle of incidence using a Bruker Vertex 70V Fourier-transform infrared (FTIR) spectrometer equipped with a combined reflection-transmission accessory, a tungsten near-infrared/visible light source, a quartz beam splitter and silicon diode detector. The measurements were performed between 80 and 320 K using a liquid nitrogen-cooled CFV2 continuous flow cryostat from Oxford Instruments. The vacuum pressures were 2 mbar for the optical path in the spectrometer and 1×10^{-6} mbar in the sample environment of the cryostat. The procedure for obtaining absorption spectra from the measured transmission and reflection spectra is described elsewhere.[41]

X-ray photoemission spectroscopy (XPS) was employed to measure the core-level spectra, valence band (VB) density of states (DoS) and secondary electron cutoff (SEC) of the Cu_3BiS_3 sample. This was achieved in a standard ultrahigh vacuum (UHV) chamber operating at a base pressure of less than 2×10^{-10} mbar, with H_2 as the main residual gas. The excitation source was Al K_α X-ray radiation, operating at 250 W. The XPS resolution is 0.38 eV as determined from the width of the Fermi edge of a polycrystalline Ag sample. Further experimental details, including the spectrometer calibration, can be found elsewhere.[42]

The sample was mounted mechanically to the sample plate and electronically to the spectrometer by means of Ta foil straps spot welded across the edges of the sample surface. In order to provide a clean surface for measurement, and to remove surface contaminants, the sample was sputtered and annealed by means of an Ar^+ ion source and a radiative heating stage. This cleaning procedure consisted of sputtering with 500 eV Ar^+ in 5 minute steps for a total of 30 minutes followed by annealing at 150°C for 1150 minutes and then at 250°C for a further 1350 minutes before allowing the sample to cool to ambient temperature. As the sample was monitored by XPS throughout, it was deemed clean when cycles of sputtering resulted in no discernible changes to the survey spectra and the peaks associated

with oxidised bismuth were no longer present in the spectra. A full set of XPS spectra was recorded both before and after the cleaning in order to demonstrate the effect of air exposure and to provide a representative VB spectrum without contamination.

To account for any sample charging, the spectra were shifted to place the peak of the C 1*s* signal (collected for many hours to obtain a sufficient signal-to-noise ratio) had a binding energy (BE) of 285.0 eV. For both before and after cleaning, this was achieved by a correction of 0.3 eV to higher binding energy, suggesting that the charging was minimal. This C 1s value is the same as that used before for this and related compounds.[18,43]

2.2 Computational methods

All of the periodic density functional theory (DFT) calculations in this article were performed through the Vienna Ab Initio Simulation Package (VASP).[44–47] The screened hybrid functional HSE06 was used for geometry optimization and density of states calculations. HSE06 includes 25% Hartree-Fock exchange, which is screened with a parameter of $w = 0.11$ Bohr^{-1}, with 75% exchange and full correlation from the generalized gradient approximation functional PBE.[48] The projector-augmented wave method was used to describe the interaction between valence and core electrons, scalar-relativistic pseudopotentials were used, and due to the presence of the heavy element Bi, spin-orbit coupling (SOC) was included for electronic structure calculations. In previous reports of $CuSbS_2$, HSE06 was used successfully without the addition of SOC,[8,29] and elsewhere SOC was shown to reduce the band gap by 30 meV without significantly changing the dispersions.[49] However, prior work on ternary bismuth chalcogenides has shown that SOC can be necessary to obtain accurate band gaps and electronic structures in comparison with experiment or higher-level GW calculations.[50] A plane wave cutoff energy of 400 eV and a Γ-centered k-point mesh of $3 \times 2 \times 4$ were used in the calculations of the electronic structure, determined to be sufficient to converge the total energy to within 1 meV atom^{-1}. A convergence criterion of 0.01 eV Å^{-1} on the forces per atom was used for geometry optimization, and the cutoff energy was increased to 560 eV

during optimization to prevent errors arising from Pulay stress.

When comparing DFT valence band DoS with XPS spectra, the contribution of inelastically scattered electrons to the data was subtracted using a Shirley background. Corrections were made to the pDoS curves for comparison with the XPS spectra. Firstly, orbitals were modulated using the standard photoionisation cross sections[51] and the curves were then convolved with a Gaussian function (0.38 eV FWHM) to account for thermal broadening and the analyser response, and then further convolved with a Lorentzian function (0.30 eV FWHM) to account for lifetime broadening. The total DoS curve is the sum of the partial curves and can now be aligned to the maximum of the most intense experimental peak in order to directly compare with experiment.

A simulated Raman spectrum was constructed using Γ-point phonon frequencies, calculated by the finite-differences method implemented in VASP, and the changes in the macroscopic dielectric tensor, calculated using Density Functional Perturbation Theory, as a result of those phonon modes using a code developed by Fonari and Stauffer.[52] Given limitations in the VASP code, these finite differences and DFPT calculations were only calculable using the PBEsol functional. To ensure sufficient accuracy in the calculation of force constants, tighter convergence criteria were used: $1\,\mathrm{meV\,Å^{-1}}$ on the forces per atom, and a higher energy cutoff of 560 eV. Optical calculations were performed using HSE06+SOC, within the method of Furthmüller and co-workers, obtaining the high-frequency real and imaginary dielectric functions, from which the absorption coefficient was derived;[53] denser k-mesh of 6 × 4 × 6 was used for these calculations to ensure accuracy.

3 Results and discussion

3.1 Crystal Structure Determination

The majority of compounds currently under investigation as PV absorbers are materials consisting of three or more elements. Therefore, they have complicated phase diagrams,

with many secondary phases. CBS is no exception. It is possible for the binary sulphides[54] and alternative stoichiometry Cu-Bi-S compounds[55] to form during growth. As such, sufficient characterisation must be undertaken to ascertain the crystalline phases present, and to exclude any secondary phases; this was achieved by XRD and Raman studies.[16,20,31,32,56–59]

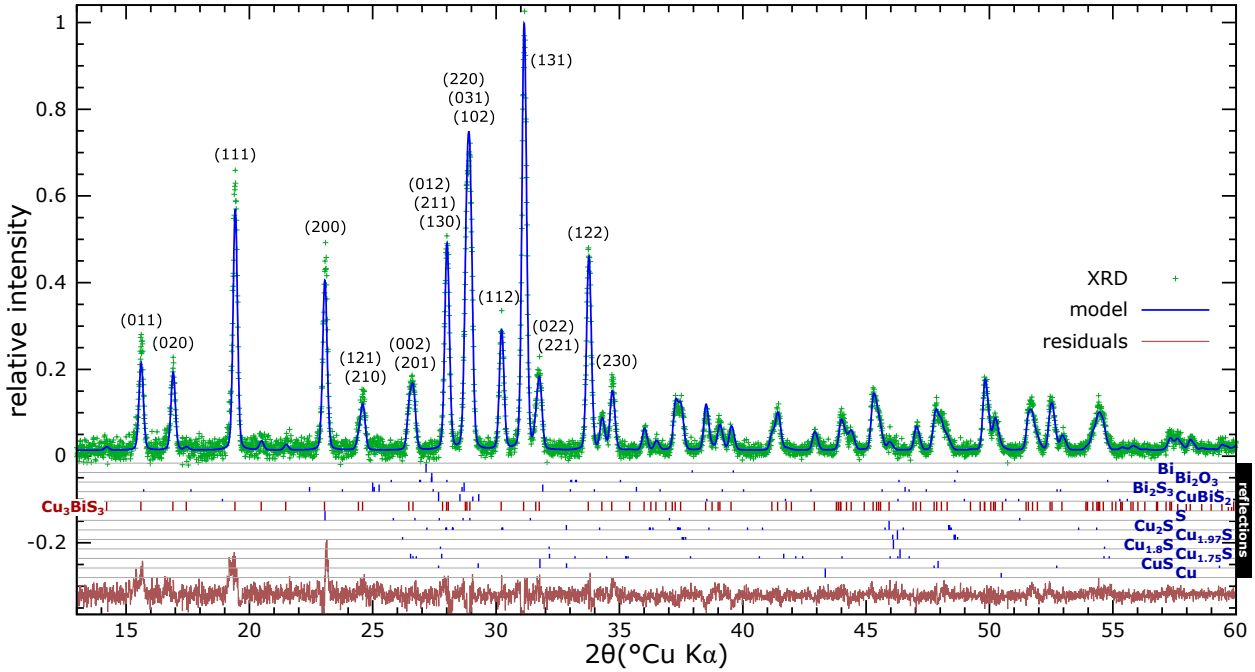

Figure 2: X-ray diffraction (Cu Kα) from the Cu_3BiS_3 film and Rietveld refinement of the Cu_3BiS_3 $P2_12_12_1$ structure. The reflection scale indicates the positions of significant reflections from potential Cu-Bi-S phases; excepting Cu_3BiS_3, the marker heights depict each pattern's relative reflection intensities (greater than 85%, 60%, 40% and 15%). Only the Cu_3BiS_3 $P2_12_12_1$ phase is well-supported by this data.

Figure Fig. 2 shows the Cu_3BiS_3 XRD pattern. Rietveld refinement of the $P2_12_12_1$ structural model of Kocman *et al.*[13] (in FullProf)[60] progressively fitted the scale factor, lattice parameters, sample displacement, lineshape parameters {U, V, W, η_0, X}, and global temperature B factor to the entire pattern, with a Pseudo-Voigt lineshape and a background described via linear interpolation through manually-selected, resolved-to-baseline control points. The refinement confirms the orthorhombic $P2_12_12_1$ structure of the film and indicates lattice parameters {a,b,c} of {7.6812(4)Å, 10.4257(5)Å, 6.7057(4)Å}, matching those reported from both a Cu_3BiS_3 thin film[56] and the wittichenite mineral[13] to within 0.5%.

The refinement assumes a random distribution of crystallite orientations, which may not hold for a polycrystalline film. While the fit suggests no significant preferential grain orientation, the residuals indicate a limited texture, yet the fit statistics do not improve satisfactorily with exponential or March-like orientation models; to avoid systematic errors, no dependent parameters were refined (e.g. atom positions or occupations). Nevertheless, the analysis indicates that the film is free of potential Cu-Bi-S impurity phases. To assess these, the pattern was evaluated against known refection positions in Cu (space group $Fm\bar{3}m$),[61] Bi ($R\bar{3}m$:R),[62] S (Fddd),[63] Bi_2S_3 (Pnma),[38] $CuBiS_2$ (Pnma),[64,65] and α-Bi_2O_3 (bismite, $P2_1/c$);[66] room-temperature relevant phases in the rich range displayed by $Cu_{2-x}S$ were also examined including Cu_2S (low-chalcocite, $P2_1/c$),[67] $Cu_{1.97}S$ (djurleite, $P2_1/n$)[67] $Cu_{1.8}S$ (low-digenite, $Fm\bar{3}m$)[68] $Cu_{1.75}S$ (anilite, Pnma),[69] and CuS ($P6_3/mmc$).[70] None of these corresponded adequately to the observed reflections as shown in Fig. 2; statistics did not improve substantially after Rietveld refinement of Cu_3BiS_3 with such impurity phases. In summary, XRD analysis indicates a phase-pure Cu_3BiS_3 ($P2_12_12_1$) film.

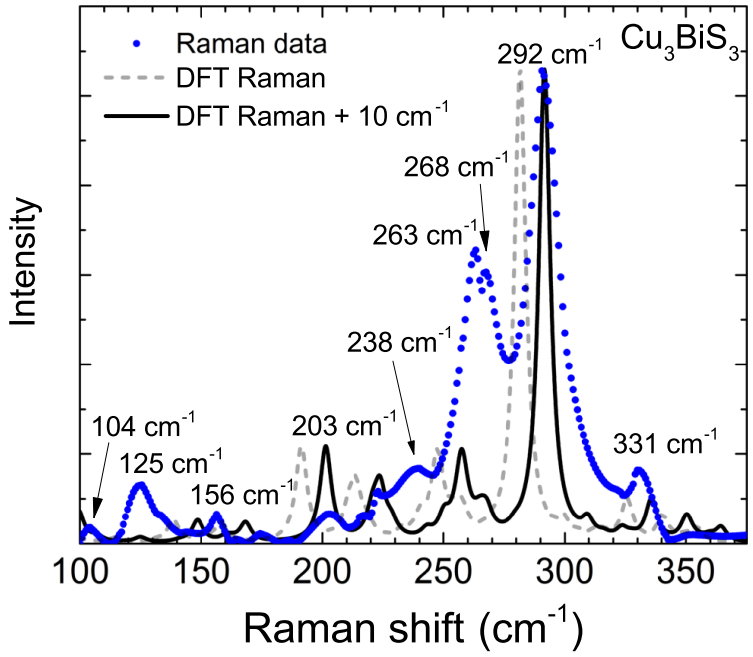

Figure 3: Raman spectrum (blue points) from a Cu_3BiS_3 film with Raman spectrum calculated from DFT (grey dashed line) and the calculated spectrum shifted by 10 cm^{-1} (black solid line).

The phase is further confirmed by agreement between experimental and calculated Raman spectra shown in Fig. 3. The experimental spectrum exhibits an intense peak at 292 cm^{-1} with two close neighboring peaks of about two-thirds the intensity at 263 and 268 cm^{-1}, consistent with noisier earlier work showing similar primary features at 292 cm^{-1} and 264 cm^{-1}.[56] In addition to previously observed peaks at 104 and 125 cm^{-1},[56] peaks at 156, 203, 238, and 331 cm^{-1} are also apparent in Fig. 3. Additionally, the Raman spectrum from Cu_3SbS_3 is very similar, but with the two most intense peaks (at 280 and 308 cm^{-1}) each 16 cm^{-1} higher than for Cu_3SbS_3 due to Sb having lower mass than Bi.[71]

The calculated Raman spectrum has peak positions around 10 cm^{-1} lower than the measured peaks. The calculated spectrum is therefore also shown after a rigid shift to 10 cm^{-1} higher frequency to account for the PBEsol functional systematically underestimating the frequencies of the optical modes. Similar small underestimations of calculated mode frequencies have been reported previously.[72,73] The calculated Raman shifts have not been scaled by a fixed percentage because Cu_3BiS_3 is orthorhombic and so the error in the lattice parameters will be different in different directions in the crystal structure. The intensity difference between experiment and theory may be due to the coarseness of the k-mesh employed in order to keep the calculations to a reasonable cost.

3.2 Core level XPS

For XPS analysis of CBS it is important to take account of the close proximity of the main peaks for Bi and S, the Bi $4f$ and S $2p$ doublets.[74] As a result, a robust fitting procedure is required to obtain an accurate analysis of the peaks. The most important XPS regions are shown here, with survey spectra shown in the SI, Fig. S1. The energies of the fit components are summarised in Table 1. A comprehensive discussion of the fitting procedure is given in the SI, together with the corroborating spectral regions and Table S1, the binding energies for all peaks, resulting from both the CBS and contaminants. The spectra presented here are normalised to enable the relative proportions of peaks due to different elements or to

different chemically shifted components to be best compared; the atomic percentages are given in Table S2.

Table 1: XPS binding energies, work function (WF) and ionisation potential (IP) for CBS before and after surface cleaning. Note that the after cleaning IP value is determined directly from the XPS to be 5.18 eV, but is revised to 4.98 eV as described in the text due to the low density of states of the topmost valence band. All values are in eV and the peak full widths at half maximum (FWHM) are given in parentheses. Binding energies of all fitted peaks in this study can be found in Table S1.

	Cu $2p_{3/2}$	Bi $4f_{7/2}$	S $2p_{3/2}$	WF	IP
Before cleaning	932.01 (1.16)	157.89 (0.65)	161.28 (0.81)	4.56	4.62
After cleaning	932.23 (1.05)	158.19 (0.77)	161.47 (0.78)	4.79	4.98

The XPS survey scans for CBS prior to and after surface cleaning are shown in Figure S1. The peaks for Cu, Bi and S are present, along with those for C and O due to atmospheric contamination which reduce significantly upon cleaning. The survey spectra additionally contain signals from sodium which diminish following cleaning. This could result from sodium diffusion from the soda lime glass - it remains after cleaning and has previously been reported.[34] The occurrence of sodium in CBS is interesting, and warrants future investigation, due to its beneficial effects on CZTS[75] and CIGS,[76] but negative impact on CdTe.[77] Further discussion of the possible effects of sodium and the other contaminants can be found in the SI along with the associated XPS spectra.

The Cu $2p$ spectra are shown in Fig. 4. They were fitted with just one doublet (red dash) both prior to and after cleaning. The doublet separation is 19.8 eV,[78] the area ratio is 1:2 and the $2p_{1/2}$ peak being broader than the $2p_{3/2}$ peak is the result of Coster-Kronig effects.[79,80] This doublet is assigned to the Cu^+ in CBS. As shown in Figure 1a, copper has three inequivalent lattice sites in CBS with the same coordination, but slightly different bond lengths and angles. Therefore, a single chemically shifted doublet component is expected to give a good fit to the copper peaks of CBS. The copper in CBS might be expected to oxidise at the surface to produce cupric oxide (CuO).[81] Such a surface species would exhibit characteristic shake-up lines in the Cu $2p$ spectra,[82] but as these are absent and the Cu $2p$

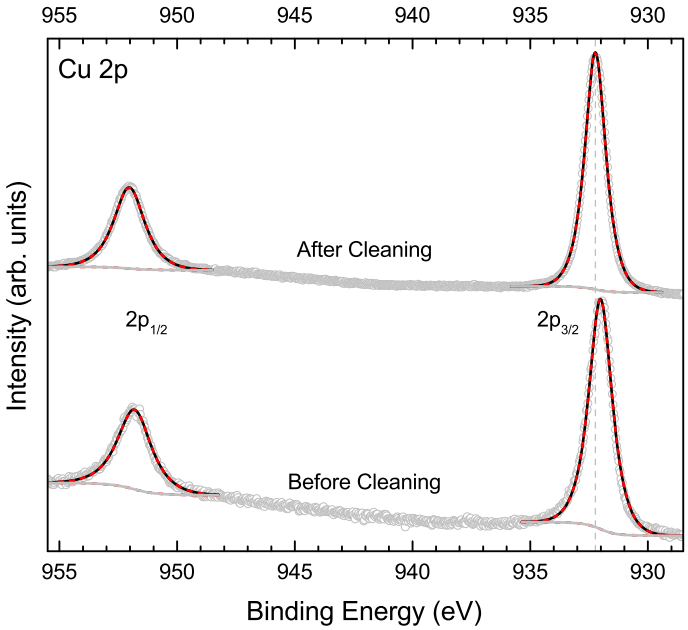

Figure 4: XPS spectra for the Cu 2p region of the CBS sample before and after surface cleaning. Fitted peaks shown in red and peak envelope in black.

spectra do not change as result of cleaning, it was determined that copper oxidation has not occurred. An additional peak, due to the Bi 4s core level, is expected to occur at a BE of around 939 eV.[83] However, this peak has not been detected because the signal is too weak and wide compared to that from Cu 2p.

The Bi 4f and S 2p core level region for CBS is shown in Fig. 5 for before and after cleaning. Curve fitting using the procedure outlined in the SI is also shown. For the Bi 4f doublet, a separation of 5.31 eV is used[83] with a 3:4 area ratio. Both before and after cleaning, the spectra contain three bismuth components. The most intense and narrowest doublet (red dash) is assigned to Bi^{3+} in the crystalline CBS. The broader Bi doublet at higher BE (pink dot) is assigned to Bi_2O_3; this component has much reduced intensity after cleaning, indicating that it corresponds to oxidised bismuth only at the surface, and is bulk not oxidised bismuth, formed during growth. The BE difference between the CBS and Bi_2O_3 is due to oxygen being more electronegative than sulphur.[84,85] It is not the result of any transformation of the oxidation state of bismuth. The attribution to Bi_2O_3 is also supported by the associated component in the O 1s spectra, shown in Figure S4b (pink dot). The oxide

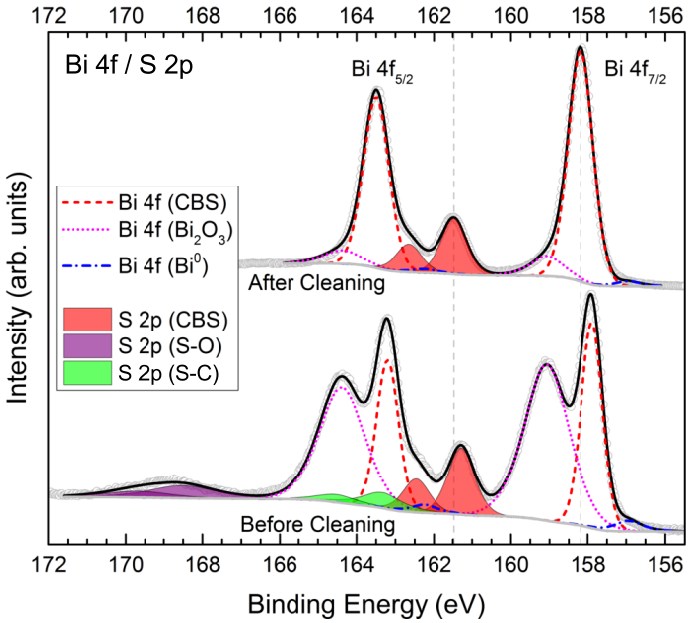

Figure 5: XPS spectra for the Bi $4f$ and S $2p$ overlap region of the CBS sample before and after surface cleaning. Peak envelope shown in black.

peak may be due to an alternative oxide, or a combination of non-stoichiometric oxides, but the Bi $4f_{7/2}$ BE is 159.1 eV which is in line with previously reported values for Bi_2O_3.[85–87] Additionally, while the Bi^{5+} oxidation state must also be considered,[88] Bi_2O_5 reportedly does not form from atmospheric contamination of bismuth.[89,90] The low intensity Bi component at lower BE (blue dash dot) to that of CBS, that diminishes upon cleaning is due to metallic Bi, as discussed in the SI where the fitting methodology is outlined. The Bi $4f_{7/2}$ peak BE of 156.9 eV is consistent with previously reported Bi metal peak positions[43,83,86,91,92] as well as our own measurements of Bi foil (see Figure S2, blue data). This is attributed to surface unreacted Bi remaining from the Bi layer deposition because its relative intensity decreases upon sputtering and annealing. If the metallic Bi resulted from sputtering or breaking of sulphur-bismuth bonds, sputtering would increase its relative intensity. However, as shown in Table S2, from the ratios of Bi from CBS and metallic Bi, the opposite occurs.

The S $2p$ doublets have a separation of 1.18 eV[93] and an area ratio of 1:2. Three sulphur species are present in the sample before cleaning, but there are only two after cleaning. The component which is removed by cleaning (purple shading) is assigned to sulphur-oxygen

bonding. This doublet is at a much higher BE (∼6 eV) than the other sulphur species. This is because it corresponds to a cation with +6 valency in contrast to the -2 valency anion nature of the other sulphide species.[94,95] The component results from reaction of the surface sulphur with atmospheric oxygen and is absent after cleaning. This S $2p$ component has previously been reported at the surface of CBS[15,20] and related sulphide absorber compounds,[96,97] but was absent where high-quality growth was reported.[36] Therefore, the presence of the sulphate species likely to be the result of sub-optimal growth conditions, involving the availability of excess sulphur for surface oxidation. The S $2p$ component at ∼163 eV (green shading) is assigned to sulphur-carbon bonding resulting from atmospheric contamination,[98] as previously reported for other sulphides.[36,42] The most intense S doublet (red shading) is assigned to sulphur in CBS with -2 valency. In Figure 1a, three distinct sulphur sites are apparent; it might therefore be expected that there would be three S doublets, corresponding to the three sites. But, even at the respectable resolution of our data, one doublet is considered to satisfactorily approximate all three sulphur species within CBS. This is not surprising as all three sites correspond to the same coordination and their bond lengths and angles are only slightly different.[8,13] The analysis of the Bi $4d$ and S $2s$ regions reported in the SI further supports the above findings and discussion.

Table 1 gives the binding energies of the CBS XPS peaks. Due to the overlapping Bi and S regions and the lack of attention to the material for applications, only a few reports of XPS from CBS exist. The measured BE of the Cu $2p_{3/2}$ peak, which is more straightforward to analyse than the Bi $4f$ and S $2p$ overlapping region, agrees several other reports of CBS. However the reported binding energies are questioned due to extremely poor SNR,[32,99,100] or the obvious presence of an additional copper component (most probably due to copper oxide) which remained unidentified due to a lack of curve fitting.[20,57] As demonstrated above, the Bi $4f$ and S $2p$ region is complicated and requires peak fitting to identify all components present. Therefore, the BE values reported in the literature for the Bi $4f_{7/2}$ and S $2p_{3/2}$ peaks vary considerably. A full discussion of the prior literature on XPS of these core levels

and its interpretation is in the SI.

Upon cleaning, all of the peaks shift to higher BE by 0.19–0.30 eV (see Table 1) as a result of movement of the Fermi level. Also, the small differences in the shifts indicate small stoichiometry changes as a result of cleaning. Indeed, surface stoichiometry values derived from XPS (detailed in Table S2) show that such changes have taken place. Prior to cleaning, there is an excess of sulphur on the surface. Following cleaning, the XPS data indicates a near stoichiometric Bi:S ratio, but a copper-deficient surface. The chemical shifts are small between different sulphides;[101] the surface is sulphur-rich before cleaning is due to partially reacted sulphur which is either desorbed or incorporated during the cleaning-related anneal. That the surface is 'copper-deficient' after cleaning is unsurprising as this has previously been reported for other Cu-based solar absorbers, including CIGS[96,102,103] and CZTS.[104,105]

3.3 Band Structure and Optical Absorption

Measured and calculated Cu_3BiS_3 optical absorption spectra are shown on a logarithmic scale in Fig. 6(a). The spectrum measured at 80 K shows an initial absorption onset at 1.18 eV, together with additional onsets at ∼1.45 and ∼1.57 eV. The calculated spectrum has been shifted down in energy by 0.35 eV to align with the experimental one; such shifts are explained as due to the omission of excitonic effects.[41,49] The measured absorption spectrum is interpreted by comparisons with the calculated spectrum, the optical transitions shown schematically in Fig. 6(b) from the top three valence bands at the Γ point, and the calculated valence band density of states (shown in Fig. 6(c)). The initial onset at 1.18 eV is assigned to direct Γ point transitions from the topmost valence band V1 to the bottom of the conduction band - the lowest direct band gap of Cu_3BiS_3. This onset is weak due to the very low density of states of the first valence band V1 in comparison to valence bands V2 and V3, see Fig. 6(c). The onsets at ∼1.45 and ∼1.57 eV correspond to the equivalent transitions from valence bands V2 and V3. There is also a direct transition associated with the band extrema at the Brillouin zone Y point - indicated on Fig. 6(a) just below the Γ point V2 transition.

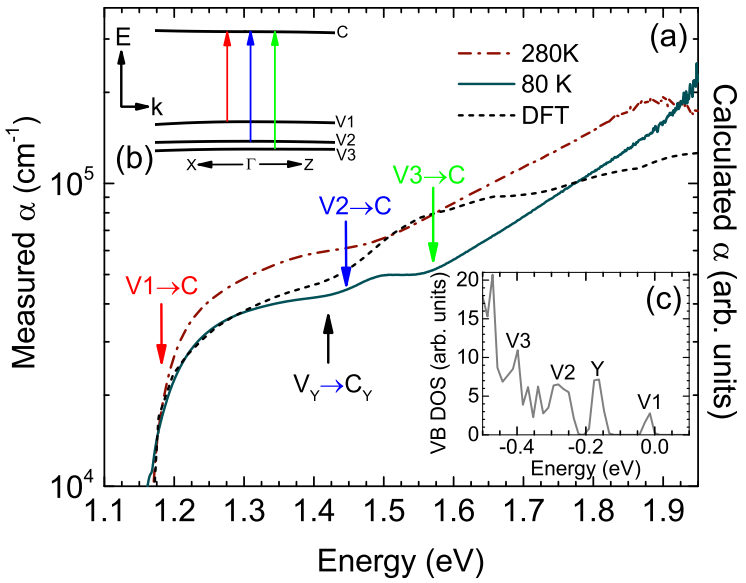

Figure 6: (a) Optical absorption spectra from Cu_3BiS_3 at 80 and 280 K plotted on a logarithmic scale; (b) Schematic representation of the band structure and absorption transitions at the Γ point; and (c) DFT density of states at the top of the valence band.

Combining this analysis of our optical data with the HSE06+SOC band structure shown in Fig. 7, indicates that Cu_3BiS_3 is a weakly indirect band gap semiconductor and that even the absorption associated with the lowest energy direct transitions at ∼1.2 eV is rather weak. Therefore, the absorption is dominated by transitions above 1.4 eV. This contrasts with several reports suggesting the band gap is direct forbidden in nature based on plots of $(\alpha h\nu)^{2/3}$ versus $h\nu$ being presented as more linear than plots with other exponents for $\alpha h\nu$, where α is the absorption coefficient.[17,21,106] According to the band structure shown in Fig. 7, there are several different critical points within a narrow energy range, making the widely used methods of analysing absorption data inappropriate for the material; it is not possible to determine the band gap of Cu_3BiS_3 by a simple linear extrapolation of $(\alpha h\nu)^n$ versus $h\nu$ for some value of n (such as 2 for direct band gap, 1/2 for indirect and 2/3 for direct forbidden). While there are interpretational differences about the nature of the band gap, Gerein and Haber report that α is 1×10^5 cm^{-1} at 1.9 eV, very similar to the absorption coefficient value being reached at 1.8 eV in our data. There is also significant absorption below their reported band gap of 1.4 eV.

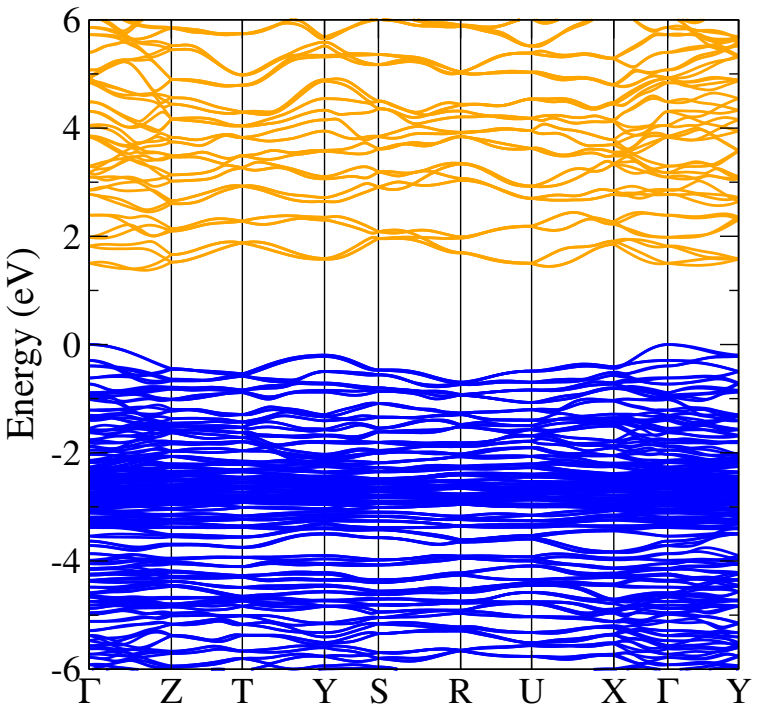

Figure 7: HSE06+SOC DFT band structure of Cu_3BiS_3; valence band is depicted in blue, conduction band in orange, and 0 eV set to valence band maximum.

In the band structure shown in Fig. 7 calculated using HSE06+SOC, the lowest direct band gap is 1.468 eV. This is at (0, 0, 0.1) - one tenth of the way along the Γ to Z direction of the Brillouin zone. The fundamental band gap is 1.372 eV and is indirect. If this difference of ∼0.1 eV is maintained when the temperature is increased from the zero Kelvin of the calculations, then the room temperature indirect gap is estimated from the absorption data to be ∼1.08 eV. The HSE06+SOC band gaps can be contrasted with the band gaps obtained using HSE06 without SOC, where the indirect band gap is 1.715 eV and the lowest direct band gap is 1.794 eV (at Γ). Therefore, in Cu_3BiS_3, the renormalisation of the band structure on the inclusion of spin-orbit coupling is significant: the fundamental gap is reduced by over 0.34 eV, a similar magnitude to that seen in other bismuth chalcogenides.[107,108] Additionally, the combination of SOC with the lack of an inversion centre results in the breaking of all band degeneracies, and causing changes in dispersion at the band edges: in centrosymmetric BiI_3, SOC has been found to improve conduction band dispersion,[109,110] here, the momentum dependent splitting leads to a lower electron effective mass and also creates additional pockets

near the CBM, which could improve the calculated absorption spectrum compared to the HSE06 electronic band structure.

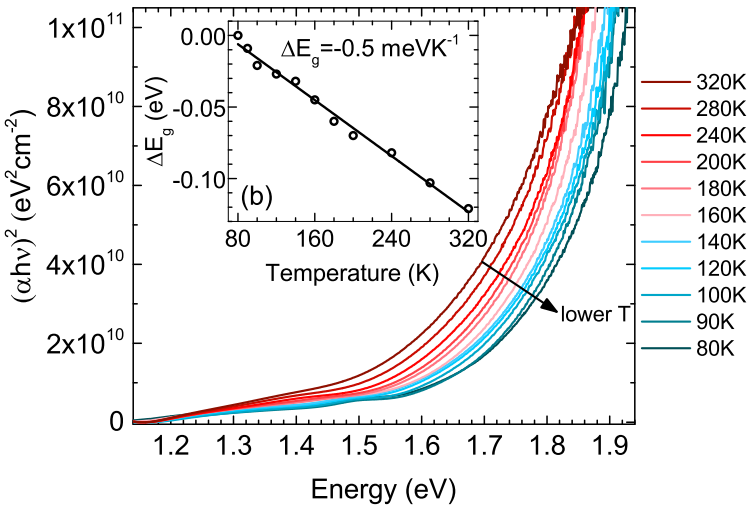

Figure 8: Optical absorption spectra from Cu_3BiS_3 between 80 and 320 K. The inset shows shift of the absorption at an $(\alpha h\nu)^2$ value of 4×10^{10} eV^{2}cm^{-2} as a function of temperature.

Temperature-dependent absorption spectra from Cu_3BiS_3 are shown in Fig. 8 where the conventional $(\alpha h\nu)^2$ versus hν plot normally used for direct allowed transitions is shown. It is clear that the curves are not linear. This *could* be interpreted as indicating that the band gap which dominates the absorption is not direct allowed, but the observed spectral shape is instead a consequence of the joint density of states of the particular band structure of Cu_3BiS_3 as indicated by the comparison in Fig. 6 between the absorption spectrum measured at 80 K and the calculated spectrum. The temperature dependence of the main absorption edge is shown in the inset of Fig. 8 and was estimated by plotting the change with temperature of the energy of the $(\alpha h\nu)^2$ versus $h\nu$ curve at 4×10^{10} eV^{2}cm^{-2}. The shift corresponds to 0.5 meVK^{-1}.

The analysis of the band gap of Cu_3BiS_3 presented here, including the temperature dependence, is consistent with the results of a previous photoreflectance study of thin films between 10 and 300 K.[56] Strong resonances were seen at ∼1.2 and ∼1.5 eV, broadly corresponding to the features seen in our absorption spectra and the transitions identified from the calculated band structure. The photoreflectance results along with our absorption spec-

tra and calculated band structure therefore indicate that the room temperature direct band gap of Cu_3BiS_3 is 1.18 eV, with an indirect band gap of ∼1.08 eV.

3.4 Band Alignment

The natural band alignment of the material,[111] was determined using photoemission, as described elsewhere.[42] Fittings of the secondary electron cutoff (SEC) and valence band maximum (VBM) for CBS are shown in Fig. 9. The measured core level binding energies, work function (WF) and ionization potential (IP) values for CBS before and after cleaning are detailed in Table 1. The measured IP and WF, along with the band gap of CBS, enable the vacuum alignment of CBS to be determined,[112] as shown in Fig. 10. The natural band offsets between CBS after cleaning, CdTe, CIGS, CZTS and the common *n*-type partner material CdS, are also shown.

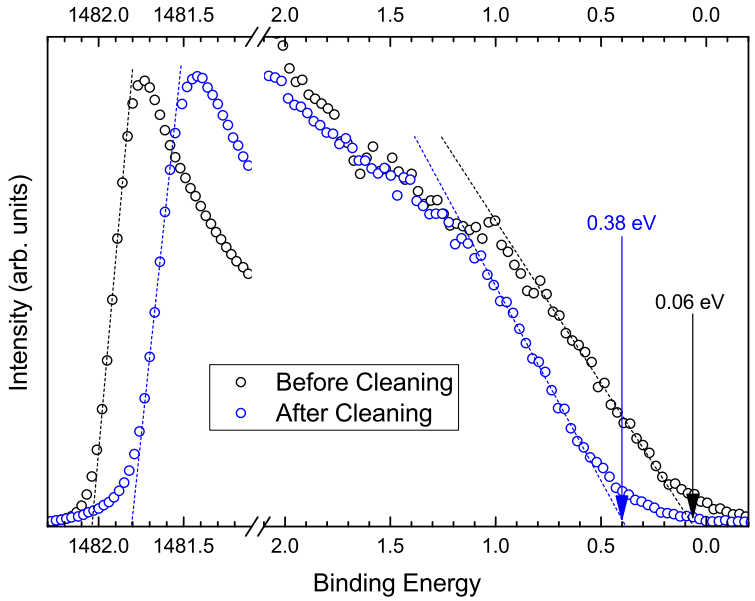

Figure 9: The secondary electron cutoff and VBM XPS spectra with linear fits for CBS before and after surface cleaning. The Fermi level is at 0 eV and the E_F to VBM energies are shown. Note the weak onset ∼0.2 eV below the extrapolated valence band edge which is discussed further in the text.

The ionisation potential obtained depends on the determined binding energy of the VBM. As discussed above in the context of the optical absorption, the density of states at the Γ

VBM is low. This means that it will not contribute significantly to the photoemission spectrum, and is evidenced by the weak onset of the valence band edge from XPS around 0.2 eV below the linearly extrapolated edge (see Figure 9). This is further supported because, according to the calculated band structure (see Figure 7), the Γ VBM is 0.2 eV above the Y VBM. Therefore, the measured ionisation potential of 5.18 eV corresponds to the separation between the valence band maximum at the Y point of the band structure and the vacuum level, and correspondingly, the fundamental ioinisation potential at the Γ point is 4.98 eV. Both of these values are represented in Figure 10, and a band gap value of 1.18 eV is shown, corresponding to the direct band gap at the Γ point: the value most appropriate for solar cell applications, given the previously analysed band structure.

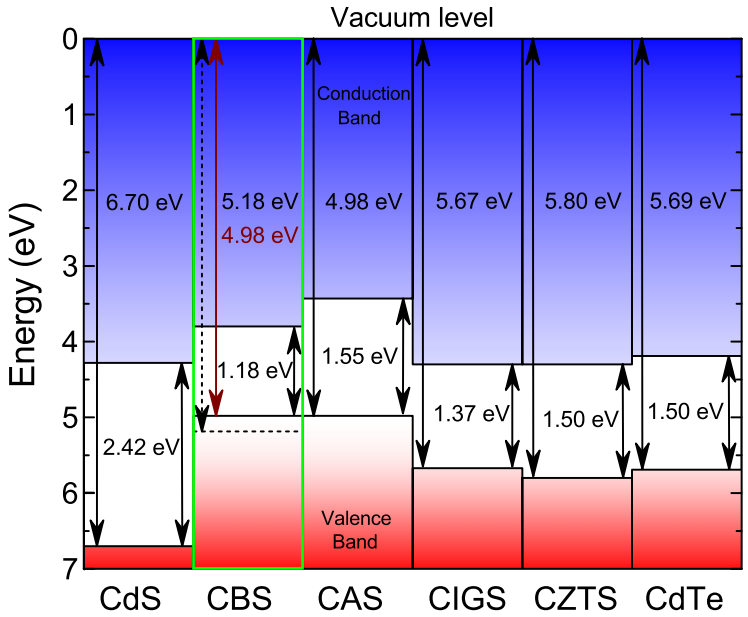

Figure 10: Vacuum-aligned band diagram between CBS and other common absorbers and the common *n*-type partner material, CdS. Literature values of ionisation potential (IP) and band gap are taken for CdS,[113] CIGS,[114] CZTS[113] and CdTe.[115] The measured IP value for CBS from XPS is 5.18 eV, but the fundamental value is 0.2 eV lower (4.98 eV) due to the low density of states of the topmost valence band at the Γ point as discussed in the text.

As shown in Table 1, after cleaning, there is a significant increase in the IP and WF. This is due to carbon contamination being removed. The presence of carbon contamination is known to reduce the IP and WF of materials.[116] Because of the understudied nature of CBS,

there are few studies of the band alignment of this compound. Only one group has reported the WF of CBS and their values are consistently lower than those determined here.[26,34,117] These reports utilised Kelvin probe force microscopy (KPFM) to measure the WF of CBS, however contamination can lower the WF, but without any in vacuo cleaning process being used. In a report which employed a chemical etch, XPS showed that the etch failed to remove substantial contamination.[34] Therefore, it appears likely that the previously reported lower WFs are due to the effects of surface contamination, particularly as KPFM averages the WF over the area being samples, while XPS gives the lowest WF in a sampled area.[118] So far, no studies except the values we present here, have reported IP values for CBS. Therefore, once cleaned, IP value for CBS reported here is representative of the material itself and small amount of residual bismuth oxide on the surface will have almost no effect.

Novel photovoltaic absorber compounds can be detrimentally affected by the use of non-optimal partner layers in device structures.[113] This arises when new materials are developed in analogy with established ones, as was the case with CZTS from CIGS.[104] CdS is often the first choice as the *n*-type partner material for new absorbers, perhaps due to its success with CIGS[119] and CdTe.[120] This raises a significant barrier against the environmental impact of an absorber such as CBS as moving away entirely from Cd-containing materials is desirable. Furthermore, from Fig. 10 it would appear that CdS would be an inappropriate choice of partner material from an electronic point of view as well, due to the large conduction band offset (CBO) between CdS and CBS, present due to the relatively low IP in comparison with CIGS and CZTS. Prior work has indicated that the best efficiences are obtained using type-I heterojunctions that have the conduction band (CB) of the *n*-type layer 0–0.4 eV above that of the absorber,[121,122] and that a recombination centre is present when there is a large CBO between CdS and CBS as shown in Fig. 10.[123] Therefore, a material with a higher conduction band minimum (CBM) and more environmentally benign elements than CdS is needed. And at the opposite side of the junction, a lower WF contact metal is probably needed. Such a approach was also required for SnS solar cells,[42,113] where the deployment of other materials

has led to positive results.[122,124] The demonstrated propensity for oxidation of CBS films, as well as literature reports of the same, shown and discussed in the data above, is a factor which should be recognised and addressed if CBS-containing devices are to be successful, with the oxidation of the surface known to have an adverse effect on cell performance in other compounds.[96,105,125] Metals oxidation produces insulators which, even when thin, can be very resistive, causing problems between layers of the solar cell and inhibiting charge carriers. In fact, bismuth oxidation has previously been reported to give a variety of different phases, with both *n*- and *p*-type conductivity,[126] large band gaps,[89,127] and high IP.[128] All these properties could be detrimental within CBS in the context of the band alignments shown in Fig. 10. XPS, with its surface sensitivity, can by used to probe such formation of surface oxide. Unlike XRD, it is able to detect both crystalline and amorpohous surface oxides and has a relatively low detection limit. Thus, we suggest that XPS can be combined effectively with other material characterisation methods such as XRD, scanning electron microscopy (SEM) and Raman spectroscopy.

3.5 Density of States

The electronic band structure of photovoltaic absorbers should be investigated in relation to understanding how bonding configurations influence the electronic properties and the prediction of how to obtain desirable properties. For corroboration with the theoretically simulated VBDoS, measurements of the valence band XPS spectra were made, which should represent the density of states well.[129,130] The experimental XPS VB spectrum from cleaned CBS is shown in Fig. 11 together with the calculated partial density of states (pDoS) in the VB.

The agreement between the calculated DoS and XPS spectra in the region at the top of the VB (I) is exceptionally good, with all features accounted for, in the correct proportions. Final state effects were unaccounted for, but it is noted that final-state relaxation will tend to cause features at the bottom of the VB to be shifted nearer to the top in XPS spectra.[129]

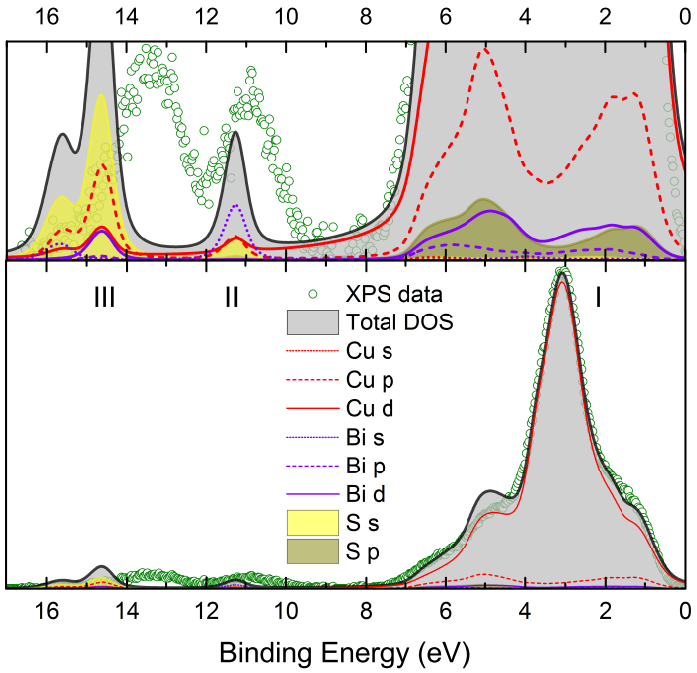

Figure 11: Calculated and experimental VB spectra for CBS (with Fermi level as the zero of the BE scale). XPS data after background subtraction are compared to broadened and corrected partial DoS curves. The magnified region shown at the top emphasises the lower intensity contributions.

This explains why the features lower in the VB (II & III) are present with approximately the correct intensities, but are shifted to lower BE in the XPS spectra.

The excellent agreement shown between the experiment and theory in Fig. 11 supports the validity of the theoretical results. However, due to the XPS spectra being dominated by Cu 3*d* states as a result of their larger cross-section, the pDoS curves before cross-section corrections were applied are also presented in Fig. 12a. This gives an improved illustration of the interactions between the orbitals present, for both the valence and conduction bands. The Cu 3*d* states remain the largest contributor to the VB, but the other orbitals can now be discerned. The Cu 3*d* states at the top of the VB (0-7 eV) are present in three different regions (IV, V, IV*), that result from the tetrahedral Cu-S bonding.

For compounds that consist of regular tetrahedral Cu-anion units, the Cu-*d* states are split by the crystal field into a non-bonding e doublet, and a t_2 triplet, that can bond with the p states of the anion. In CBS, the observed DoS is closely related to that of regular

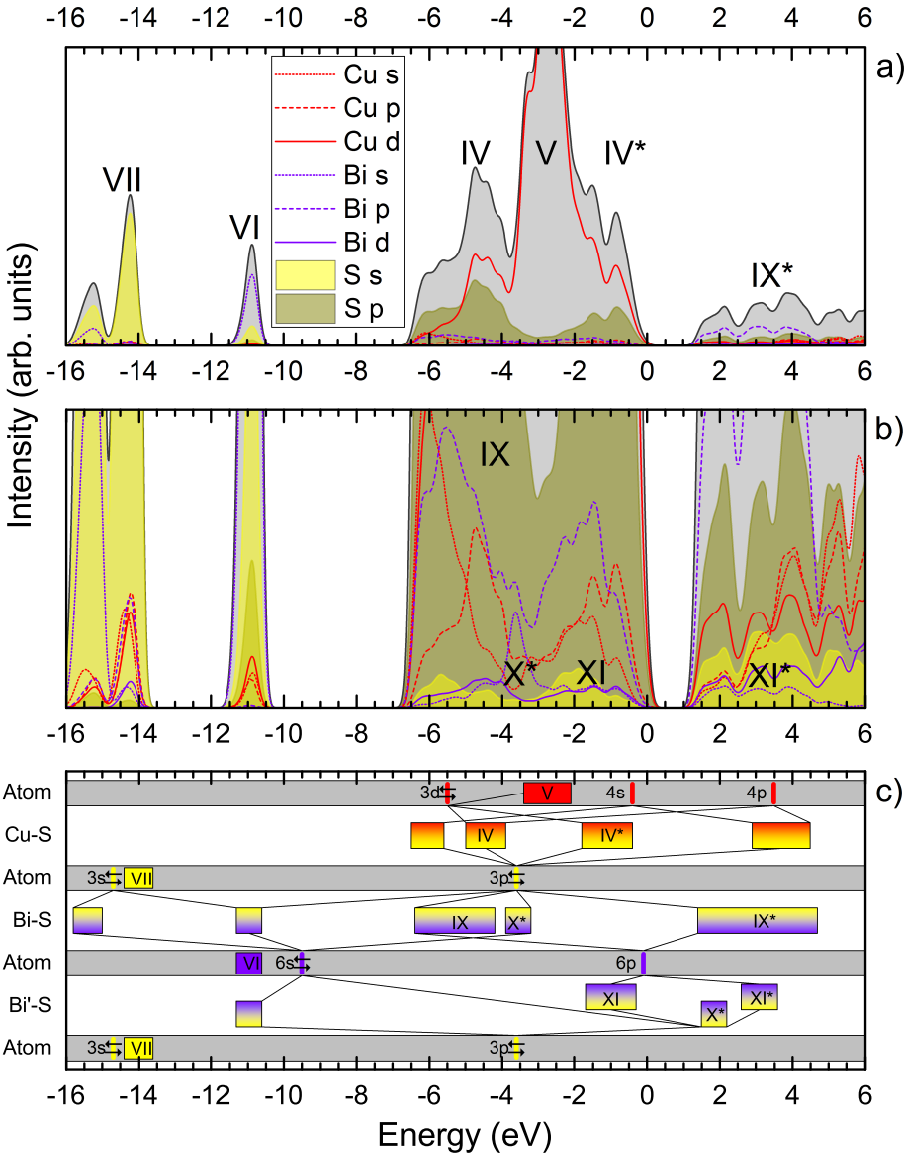

Figure 12: a) & b) Total and partial electronic density of states curves for CBS, with intensity zoomed region to more clearly show the underlying orbitals. Curves have been convolved with a Gaussian function (0.3 eV FWHM) in order to better distinguish features. DoS curves are aligned to the VBM. Black curve with grey shading is the total summed DoS. c) Configuration energies for the valence orbitals[131,132] displayed with a schematic of the bonding hybridisations as discussed in the text. It is noted that the CE values do not take ionisation, multi-electron occupancy or hybridisation into account and are shown only as a schematic guide. Part labels are discussed and referred to throughout the text.

tetrahedral compounds since its distorted Cu-S units are derived from tetrahedra.[133,134] This results in an intense central peak (V) comprised solely of the non-bonding e Cu-d states with two weaker features (IV, IV*) on either side, representing the Cu-d t_2 orbitals mixed with S-p orbitals (bonding and antibonding states respectively). However, due to the Cu-S units being highly distorted, the relative proportions of bonding and non-bonding states differ from regular tetrahedra and additional shoulders and peaks are apparent in the DoS as a result of the crystal distortion. Some hybridisation is forbidden in contrast to it being symmetry allowed in non-distorted structures. This is corroborated by the fact that the top of the VB of CBS is more similar to that of Cu_2S[135] (highly distorted tetrahedra) than to CAS[29,36] (near-regular tetrahedra).

At higher BE energy are two other distinct regions: one around 11 eV (VI) comprising mostly Bi-s states, and the other between 14 and 16 eV (VII) containing mainly S-s states. The orbital configuration energies (CEs) are presented in Fig. 12c. The Bi 6s and S 3s orbitals are semi-localised as indicated by their intense features VI and VII and the absence of these orbitals at the top of the VB. Antibonding states consisting mostly of Bi-p hybridized with S-p (IX*) dominate the CBM and the first conduction band. The corresponding bonding states occur throughout the VB, in addition to the Cu-d contributions (IX).

Additional understanding of the nature of the bonding can be obtained from investigating the Bi cation-related states at the band extrema. This is apparent in the zoomed-in DoS, shown in Figure 12b. As a result of there being three times more Cu atoms than Bi atoms in CBS and the resulting strength of the Cu-related features, the states due to Bi hybridization are relatively weak. In spite of this, their presence can significantly influence the properties. Within the $Cu_3(As,Sb,Bi)(S,Se)_3$ family of materials, it has been proposed that the contribution of cation-s states to the top of the VB diminishes upon going down group V to Bi.[8] This is due to the increasing separation and reduced interaction of the cation-s and anion-p orbitals as the group is descended. The Bi-s states initially seem only to be in the VB as a result of the anti-bonding hybridisation with S-p states (X*). However, a more detailed

look reveals a contribution to the conduction band (XI*) from Bi-s states and its intensity is similar to that close to the VBM (XI). This intensity therefore indicates that there is some degree of mixing of the Bi-s states according to the revised lone pair model[136] and the antibonding Bi-s/S-p states (X*) further mix with the Bi-p orbitals due to their proximity, resulting in full bonding states near the VBM (XI). This bonding scheme is depicted on the orbital diagram in Fig. 12c. However, this hybridization is not as strong as seen in other lone-pair active materials. This weaker interaction is expected and is therefore thought not to contribute significantly to the material's properties. This is manifested in the structure, by comparison with other lone-pair active compounds.[136] The voids into which the lone pair electron density is projected are smaller in CBS than in the other materials. The other states that contribute significantly to the valence and conduction bands are further detailed in the schematic bonding diagram in Fig. 12c.

Prior DFT studies of CBS concentrated on the band structure and the relation to the optical spectra,[22,56,137] with a single investigation discussing the nature of bonding, but without relating it to the band alignments.[8] The pDoS in prior work are in general agreement with those presented here. One report highlighted that the s-like nature of the VBM for these materials with a group V^{3+} cation gives enhanced absorption compared with a group V^{5+} cation, and higher absorption than CIGS.[137] This favourable optical property is one of the motivations for increased interest in these materials.

While the optical properties of CBS have been measured and calculated in quite a few studies and have been found to be compatible with solar cell potential, the band alignments, that enable the design of device architecture, have received much less attention. The IP value determined will inform the future design of CBS-based cells. As the IP of CBS found here is not as high as for other common absorbers, as has been discussed in the previous section, CBS will likely need more suitable partner layer materials within a solar cell structure. From the perspective of orbitals and bonding, it is apparent that this low IP is inherent to this material family and is due to the unusual bonding configuration when compared to other

absorbers. Hereafter, reference is made to Fig. 13 for the valence orbital relative energies for the elements of common thin film solar absorbers and their occupancy in the materials, according to their formal ionic oxidation states.

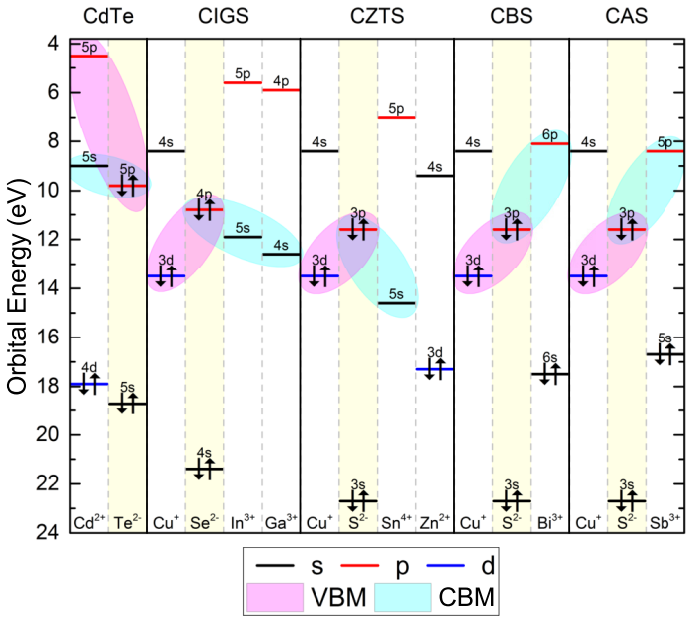

Figure 13: Configuration energies[131,132] for the valence orbitals of common solar absorbers CdTe, CIGS, CZTS and the new absorber CBS and CAS. The formal occupancy of the orbitals within the compunds is depicted and the main orbitals are shown which contribute to the VBM and CBM. The Cd-p levels is shown at an estimated value according to the trend from Sn and In.

CdTe is an 'archetypical II-VI' material with a VBM mostly comprising bonding cation-p/anion-p states and a CBM mostly comprising antibonding cation-s/anion-p states, with the corresponding antibonding (bonding) states occurring higher (lower) in the CB (VB) with respect to the band edge.[138,139] The cation-d orbitals of CdTe are bound too strongly to significantly interact with valence states and therefore do not influence the VBM. However, in the copper-containing compounds (CIGS, CZTS, CAS, CBS), the full Cu-d states are close in energy to the full anion-p orbitals. Therefore the copper-d/anion-p states dominate the VB of these compounds as detailed above. This is advantageous for solar cells, as the copper vacancy is a shallow acceptor responsible for the inherent p-type conductivity of these compounds,[8,140–142] the high-lying Cu-d level tends to produce a VBM that favours junction

formation and Ohmic contacting,[143] and the antibonding states at the VBM have been suggested to result in defect-tolerance.[144] The binary Cu-chalcogenide Cu_2S lacks stability, which can be enhanced by adding another cation with an empty valence d-band, generating the conduction band and hence preventing copper illumination-induced self-reduction.[145] These features will also apply to CBS. In spite of the differences between the VB of CdTe and the copper-based materials, the CBMs are simlar for CdTe, CIGS and CZTS. They consist of antibonding non-Cu-cation-s/anion-p states, that are energetically in quite close proximity (Fig. 13).

CBS DoS superficially resembles that of both CZTS and CIGS in that they share the same main Cu-d/anion-p domination of the VB. However, their CB states differ substantially, and, when studied in detail, the VB states differ too (shown in Fig. 12 and Fig. 13). This is the reason for the low IP in comparison with other PV materials. This is mostly due to the electronic structure of the non-Cu-cation. This is $(In/Ga)^{3+}$ in CIGS and Sn^{4+} in CZTS, that have valence-s orbitals which are formally unoccupied and close to the formally occupied anion-p orbitals. The hybridisation of these levels cause the antibonding states to form the CBM, while the bonding states lie deeper in the VB, beneath the Cu-d states at the VBM. However, the non-Cu-cation is Bi^{3+} in CBS with its more tightly bound, formally occupied valence-s orbitals, and it is the less strongly bound valence-p orbitals that are energetically near to the anion-p orbitals. Therefore, due to the energetic differences apparent in Fig. 13, the Bi-p/S-p antibonding states go on to make up the CBM of CBS, whereas the bonding states are shallower in the VB, and overlap to some degree with the Cu-d states. Additionally, there is a small contribution from Bi-s states at the VBM due to the previously described revised lone pair mechanism. These additional states alter the band alignments, raising the VBM somewhat, marginally lowering the IP, and generating band misalignment with other absorbers, seen in Fig. 10, which is thought to be substantial in its effects in PV devices. In CIGS and CZTS, the non-Cu-cation-s/anion-p hybridized bonding states occur a lot deeper in the VB and have no overlap with the Cu-d states and no contribution to the VBM; this

increases the IP.[133,146] As a result of the similarities with CAS,[36] it is clear that this bonding regime is an inherent characteristic of this materials family.

Therefore, both in this family of materials, and possibly extended to future materials, the band levels and the bonding nature of the VB and CB can be somewhat predicted from the orbital levels. That is, if the cation-*d* orbitals are occupied and are energetically close to the anion-*p* orbital (e.g. Cu^+), then the VB will be dominated by the mixing of these states and the CB will probably comprise the antibonding mixture of anion-*p* with the most tightly bound, formally unoccupied cation orbital. Trends of the VBM positions for common-cation and common-anion materials have been shown to be predicted correctly for binary compounds,[147,148] considering a simple tight-binding model with regards to the relative positions of the elemental atomic orbital levels. However, such an approach is inapplicable here as the multi-component nature of the materials adds an extra dimension of complexity, and the differences in crystal structure also play a role. As such, CZTS/CIGS and CBS cannot be directly compared using this approach. It may however be the case that such a model is applicable within the family of materials, for example, comparing Cu_3BiS_3 and Cu_3BiSe_3, when development reaches that stage.

Still, the understanding of orbital interactions and band alignments obtained here, coupled with previous findings that this family of materials has been shown to demonstrate far superior absorption to that of CIGS,[137] and that both of these features are understood to be due to the nature of the bonding, all suggest some optimism for the use of CBS. The better performance of CIGS over CBS may not be the result of inherent problems with CBS, but instead the greater development time that CIGS has enjoyed. CBS retains significant potential as a solar PV absorber, but could require substantial further research into material synthesis and cell design.

4 Conclusions

We have presented a thorough XPS spectral analysis of the Cu_3BiS_3 core-levels, and developed a model which disambiguates spectral complexities, particularly those resulting from overlap of the Bi $4f$ and S $2p$ lines.

Optical absorption spectra and first principles calculations determine a ∼1.2 eV direct band gap rather than the often-reported 1.4-1.5 eV; this discrepancy is due to the low density of states of the topmost valence band.

The Cu_3BiS_3 ionisation potential (4.98 eV) is reported for the first time: indicating band edges which are too high for CdS to be a suitable solar cell p-n-junction partner, and that alternative n-type layers are required. Models fitted to the experimental valence band spectra and theoretical density of states substantiate the analysis of the bonding in CBS. A major contribution to the valence band maximum is from Cu-d and S-p states, but Bi-p states also play a role; this differs from CIGS and CZTS, and is partly why a low IP value is determined here. The implications of the Bi-6s lone-pair electrons are also discussed; the conduction band's Bi-p character arises from the trivalent Bi (with full valence s- and empty valence p-states), again different from the non-Cu cation (with empty valence s-states) in CIGS or CZTS. This understanding does not dampen the potential of CBS, but direct comparisons with well-developed PV absorbers should be avoided, and new device architectures explored.

Acknowledgement

The authors thank the UK Engineering and Physical Sciences Research Council (EPSRC). TJW and PAEM acknowledge funding through EPSRC studentships (Grant Nos EP/K503095/1, EP/L505018/1, and EP/N509693/1). PJY and KD acknowledge funding through the EPSRC Centre for Doctoral Training in New and Sustainable Photovoltaics (EP/L01551X/1). JDM acknowledges funding from EPSRC grant no. EP/N014057/1 and TDV, MB and VRD from EP/N015800/1. The XRD facility was funded by the University of Liverpool and the

EPSRC under Grant No. EP/P001513/1. The DFT calculations in this article made use of the ARCHER U.K. National Supercomputing Service (http://www.archer.ac.uk), via our membership of the U.K.s HEC Materials Chemistry Consortium, which is funded by EPSRC (Grant No. EP/L000202/1), and the UCL Legion (Legion@UCL) and Grace (Grace@UCL) HPC Facilities. DOS acknowledges funding through EPSRC (Grant No. EP/N01572X/1) and CNS is grateful to EPSRC and the Department of Chemistry at UCL for the provision of a Doctoral Training Partnership studentship (ref No. 1492829). DOS and TDV acknowledge membership of the Materials Design Network.

Supporting Information Available

Details of surface contamination, stoichiometry measurements, XPS core level fitting procedure for Bi and S and comparisons with previous literature.

This material is available free of charge via the Internet at `http://pubs.acs.org/`.

References

(1) Green, M. A.; Emery, K.; Hishikawa, Y.; Warta, W.; Dunlop, E. D. Solar Cell Efficiency Tables (Version 48). *Prog. Photovoltaics Res. Appl.* **2016**, *24*, 905–913.

(2) Polman, A.; Knight, M.; Garnett, E. C.; Ehrler, B.; Sinke, W. C. Photovoltaic Materials Present Efficiencies and Future Challenges. *Science* **2016**, *352*, 307.

(3) Wadia, C.; Alivisatos, A. P.; Kammen, D. M. Materials Availability Expands the Opportunity for Large-Scale Photovoltaics Deployment. *Environ. Sci. Technol.* **2009**, *43*, 2072–2077.

(4) Siebentritt, S. Why Are Kesterite Solar Cells Not 20% Efficient? *Thin Solid Films* **2013**, *535*, 1–4.

(5) Siebentritt, S.; Schorr, S. Kesterites-a Challenging Material for Solar Cells. *Prog. Photovoltaics Res. Appl.* **2012**, *20*, 512–519.

(6) Yin, L.; Cheng, G.; Feng, Y.; Li, Z.; Yang, C.; Xiao, X. Limitation Factors for the Performance of Kesterite Cu_2ZnSnS_4 Thin Film Solar Cells Studied by Defect Characterization. *RSC Adv.* **2015**, *5*, 40369–40374.

(7) Kumar, M.; Dubey, A.; Adhikari, N.; Venkatesan, S.; Qiao, Q. Strategic Review of Secondary Phases, Defects and Defect-Complexes in Kesterite CZTSSe Solar Cells. *Energy Environ. Sci.* **2015**, *8*, 3134–3159.

(8) Kehoe, A. B.; Temple, G. W., D. J. and Watson; Scanlon, D. O. Cu_3MCh_3 (M = Sb, Bi; Ch = S, Se) as Candidate Solar Cell Absorbers: Insights from Theory. *Phys. Chem. Chem. Phys.* **2013**, *15*, 15477.

(9) Ganose, A. M.; Savory, C. N.; Scanlon, D. O. Beyond methylammonium lead iodide: prospects for the emergent field of ns^2 containing solar absorbers. *Chem. Commun.* **2017**, *53*, 20–44.

(10) Peccerillo, E.; Durose, K. Copper-antimony and copper-bismuth chalcogenides - Research opportunities and review for solar photovoltaics. *MRS Energy & Sustainability* **2018**, *5*, E13.

(11) U.S. Geological Survey. Mineral Commodity Summaries 2016.

(12) Hintze, C. A. F. *Handbuch Der Mineralogie*; Cambridge, 1904.

(13) Kocman, V.; Nuffield, E. W. The Crystal Structure of Wittichenite, Cu_3BiS_3. *Acta Crystallogr. Sect. B Struct. Crystallogr. Cryst. Chem.* **1973**, *29*, 2528–2535.

(14) Nuffield, E. W. Studies of Mineral Sulpho-Salts: Xi-Wittichenite (Klaprothite). *Econ. Geol.* **1947**, *42*, 147–160.

(15) Nair, P. K.; Huang, L.; Nair, M. T. S.; Hu, H.; Meyers, E. A.; Zingaro, R. A. Formation of p-Type Cu_3BiS_3 Absorber Thin Films by Annealing Chemically Deposited Bi_2S_3-CuS Thin Films. *J. Mater. Res.* **1997**, *12*, 651–656.

(16) Colombara, D.; Peter, L. M.; Hutchings, K.; Rogers, K. D.; Schäfer, S.; Dufton, J. T. R.; Islam, M. S. Formation of Cu_3BiS_3 Thin Films via Sulfurization of BiCu Metal Precursors. *Thin Solid Films* **2012**, *520*, 5165–5171.

(17) Gerein, N. J.; Haber, J. A. One-Step Synthesis and Optical and Electrical Properties of Thin Film Cu_3BiS_3 for Use as a Solar Absorber in Photovoltaic Devices. *Chem. Mater.* **2006**, *18*, 6297–6302.

(18) Mesa, F.; Dussan, A.; Gordillo, G. Study of the Growth Process and Optoelectrical Properties of Nanocrystalline Cu_3BiS_3 Thin Films. *Phys. Stat. Sol. (c)* **2010**, *7*, 917–920.

(19) Mesa, F.; Gordillo, G. Effect of Preparation Conditions on the Properties of Cu_3BiS_3 Thin Films Grown by a Two Step Process. *J. Phys. Conf. Ser.* **2009**, *167*, 12019.

(20) Murali, B.; Madhuri, M.; Krupanidhi, S. B. Near-Infrared Photoactive Cu_3BiS_3 Thin Films by Co-Evaporation. *J. Appl. Phys.* **2014**, *115*, 173109.

(21) Estrella, V. N.; Nair, M. T. S.; Nair, P. K. Semiconducting Cu_3BiS_3 Thin Films Formed by the Solid-State Reaction of CuS and Bismuth Thin Films. *Semicond. Sci. Technol.* **2003**, *18*, 190–194.

(22) Kumar, M.; Persson, C. Cu_3BiS_3 as a Potential Photovoltaic Absorber with High Optical Efficiency. *Appl. Phys. Lett.* **2013**, *102*, 3–7.

(23) Gerein, N.; Haber, J. Synthesis and Optical and Electrical Properties of Thin Films Cu_3BiS_3-A Potential Solar Absorber for Photovoltaic Devices. IEEE 4th World Conference on Photovoltaic Energy. 2006; pp 564–566.

(24) Gerein, N.; Haber, J. Cu_3BiS_3, Cu_3BiS_4, Ga_3BiS_3 and $Cu_5Ga_2BiS_8$ as Potential Solar Absorbers for Thin Film Photovoltaics. Proceedings of the of the Thirty-first IEEE Photovoltaic Specialists Conference. 2005; pp 159–162.

(25) Mesa, F.; Dussan, A.; Sandino, J.; Lichte, H. Characterization of Al/Cu_3BiS_3/buffer/ZnO Solar Cells Structure by TEM. *J. Nanoparticle Res.* **2012**, *14*, 1054.

(26) Mesa, F.; Fajardo, D. Study of Heterostructures of Cu_3BiS_3 buffer Layer Measured by Kelvin Probe Force Microscopy Measurements (KPFM). *Can. J. Phys.* **2014**, *92*, 892–895.

(27) Li, J.; Han, X.; Zhao, Y.; Li, J.; Wang, M.; Dong, C. Onestep synthesis of Cu_3BiS_3 thin films by a dimethyl sulfoxide (DMSO)-based solution coating process for solar cell application. *Sol. Energy Mat. Sol. Cells* **2018**, *174*, 593–598.

(28) Deshmukh, S. G.; Kheraj, V. A comprehensive review on synthesis and characterizationsof Cu_3BiS_3 thin films for solar photovoltaics. *Nanotechnol. Environ. Eng.* **2017**, *2*, 15.

(29) Temple, D. J.; Kehoe, A. B.; Allen, J. P.; Watson, G. W.; Scanlon, D. O. Geometry, Electronic Structure, and Bonding in $CuMCh_2$ (M = Sb, Bi; Ch = S, Se): Alternative Solar Cell Absorber Materials? *J. Phys. Chem. C* **2012**, *116*, 7334–7340.

(30) Rodriguez-Lazcano, Y.; Nair, M. T. S.; Nair, P. K. $CuSbS_2$ Thin Film Formed through Annealing Chemically Deposited Sb_2S_3-CuS Thin Films. *J. Cryst. Growth* **2001**, *223*, 399–406.

(31) Hu, H.; Gomez-Daza, O.; Nair, P. K. Screen-Printed Cu_3BiS_3-Polyacrylic Acid Composite Coatings. *J. Mater. Res.* **1998**, *13*, 2453–2456.

(32) Hu, J.; Deng, B.; Wang, C.; Tang, K.; Qian, Y. Convenient Hydrothermal Decomposition Process for Preparation of Nanocrystalline Mineral Cu_3BiS_3 and $Pb_{1-x}Bi_{2x/3}S$. *Mater. Chem. Phys.* **2003**, *78*, 650–654.

(33) Gerein, N. J.; Haber, J. A. Synthesis of Cu_3BiS_3 Thin Films by Heating Metal and Metal Sulfide Precursor Films under Hydrogen Sulfide. *Chem. Mater.* **2006**, *18*, 6289–6296.

(34) Mesa, F.; Chamorro, W.; Vallejo, W.; Baier, R.; Dittrich, T.; Grimm, A.; Lux-Steiner, M. C.; Sadewasser, S. Junction Formation of Cu_3BiS_3 Investigated by Kelvin Probe Force Microscopy and Surface Photovoltage Measurements. *Beilstein J. Nanotechnol.* **2012**, *3*, 277–284.

(35) Septina, W.; Ikeda, S.; Iga, Y.; Harada, T.; Matsumura, M. Thin Film Solar Cell Based on $CuSbS_2$ Absorber Fabricated from an Electrochemically Deposited Metal Stack. *Thin Solid Films* **2014**, *550*, 700–704.

(36) Whittles, T. J.; Veal, T. D.; Savory, C. N.; Welsch, W.; de Souza Lucas, F. W.; Gibbon, J. T.; Birkett, M.; Potter, R. J.; Scanlon, D. O.; Zakutayev, A.; Dhanak, V. R. Core Levels, Band Alignments, and Valence-Band States in $CuSbS_2$ for Solar Cell Applications. *ACS Appl. Mater. Interfaces* **2017**, *9*, 41916–41926.

(37) Schorr, S. Structural Aspects of Adamantine like Multinary Chalcogenides. *Thin Solid Films* **2007**, *515*, 5985–5991.

(38) Lundegaard, L. F.; Makovicky, E.; Boffa-Ballaran, T.; Balic-Zunic, T. Crystal Structure and Cation Lone Electron Pair Activity of Bi_2S_3 between 0 and 10 GPa. *Phys. Chem. Miner.* **2005**, *32*, 578–584.

(39) Caracas, R.; Gonze, X. First-Principles Study of the Electronic Properties of A_2B_3 Minerals, with A=Bi,Sb and B=S,Se. *Phys. Chem. Miner.* **2005**, *32*, 295–300.

(40) Evans, H. T. Crystal Structure of Low Chalcocite. *Nat. Phys. Sci.* **1971**, *232*, 68–70.

(41) Birkett, M.; Savory, C. N.; Fioretti, A. N.; Thompson, P.; Muryn, C. A.; Weerakkody, A. D.; Mitrovic, I. Z.; Hall, S.; Treharne, R.; Dhanak, V. R.; Scanlon, D. O.; Zakutayev, A.; Veal, T. D. Atypically Small Temperature-Dependence of the Direct Band Gap in the Metastable Semiconductor Copper Nitride Cu_3N. *Phys. Rev. B* **2017**, *95*, 115201.

(42) Whittles, T. J.; Burton, L. A.; Skelton, J. M.; Walsh, A.; Veal, T. D.; Dhanak, V. R. Band Alignments, Valence Bands, and Core Levels in the Tin Sulfides SnS, SnS_2, and Sn_2S_3: Experiment and Theory. *Chem. Mater.* **2016**, *28*, 3718–3726.

(43) Morgan, W. E.; Stec, W. J.; van Wazer, J. R. Inner-Orbital Binding Energy Shifts of Antimony and Bismuth Compounds. *Inorg. Chem.* **1972**, *12*, 953–955.

(44) Kresse, G.; Hafner, J. *Ab initio* molecular dynamics for liquid metals. *Phys. Rev. B* **1993**, *47*, 558(R).

(45) Kresse, G.; Hafner, J. *Ab initio* molecular-dynamics simulation of the liquid-metalamorphous-semiconductor transition in germanium. *Phys. Rev. B* **1994**, *49*, 14251.

(46) Kresse, G.; Furthmüller, J. Efficiency of ab-initio total energy calculations for metals and semiconductors using a plane-wave basis set. *Computational Materials Science* **1996**, *6*, 15.

(47) Kresse, G.; Furthmüller, J. Efficient iterative schemes for ab initio total-energy calculations using a plane-wave basis set. *Phys. Rev. B* **1996**, *54*, 11169.

(48) Krukau, A. V.; Vydrov, O. A.; Izmaylov, A. F.; Scuseria, G. E. Influence of the exchange screening parameter on the performance of screened hybrid functionals. *J. Chem. Phys.* **2006**, *125*, 224106.

(49) Birkett, M.; Savory, C. N.; Rajpalke, M. K.; Linhart, W. M.; Whittles, T. J.; Gibbon, J. T.; Welch, A. W.; Mitrovic, I. Z.; Zakutayev, A.; Scanlon, D. O.; Veal, T. D. Band gap temperature-dependence and exciton-like state in copper antimony sulphide, $CuSbS_2$. *APL Materials* **2018**, *6*, 084904.

(50) Savory, C. N.; Ganose, A. M.; Scanlon, D. O. Exploring the PbS-Bi_2S_3 Series for Next Generation Energy Conversion Materials. *Chem. Mater.* **2017**, *29*, 5156–5167.

(51) Yeh, J. J.; Lindau, I. Atomic Subshell Photoionization Cross Sections and Asymmetry Parameters: $1 \leq Z \leq 103$. *At. Data Nucl. Data Tables* **1985**, *32*, 1–155.

(52) Fonari, A.; Stauffer, S. *vasp_raman.py*; https://github.com/raman-sc/VASP/, 2013.

(53) Gajdoŝ, M.; Hummer, K.; Kresse, G.; Furthmüller, J.; Bechstedt, F. Linear optical properties in the projector-augmented wave methodology. *Phys. Rev. B* **2006**, *73*, 045112.

(54) Colombara, D.; Peter, L. M.; Rogers, K. D.; Hutchings, K. Thermochemical and Kinetic Aspects of the Sulfurization of CuSb and CuBi Thin Films. *J. Solid State Chem.* **2012**, *186*, 36–46.

(55) Wang, N. The Cu-Bi-S System: Results from Low-Temperature Experiments. *Mineral. Mag.* **1994**, *58*, 201–204.

(56) Yakushev, M. V.; Maiello, P.; Raadik, T.; Shaw, M. J.; Edwards, P. R.; Krustok, J.; Mudryi, A. V.; Forbes, I.; Martin, R. W. Electronic and Structural Characterisation of Cu_3BiS_3 Thin Films for the Absorber Layer of Sustainable Photovoltaics. *Thin Solid Films* **2014**, *562*, 195–199.

(57) Zhong, J.; Xiang, W.; Cai, Q.; Liang, X. Synthesis, Characterization and Optical Properties of Flower-like Cu_3BiS_3 Nanorods. *Mater. Lett.* **2012**, *70*, 63–66.

(58) Liu, J.; Wang, P.; Zhang, X.; Wang, L.; Wang, D.; Gu, Z.; Tang, J.; Guo, M.; Cao, M.; Zhou, H.; Liu, Y.; Chen, C. Rapid Degradation and High Renal Clearance of Cu_3BiS_3 Nanodots for Efficient Cancer Diagnosis and Photothermal Therapy in Vivo. *ACS Nano* **2016**, *10*, 4587–4598.

(59) Yan, C.; Gu, E.; Liu, F.; Lai, Y.; Li, J.; Liu, Y. Colloidal Synthesis and Characterizations of Wittichenite Copper Bismuth Sulphide Nanocrystals. *Nanoscale* **2013**, *5*, 1789–1792.

(60) Rodríguez-Carvajal, J. Recent advances in magnetic structure determination by neutron powder diffraction. *Physica B* **1993**, *192*, 55–69.

(61) Su, I.-K.; Ohta, H.; Waseda, Y. High-temperature thermal expansion of six metallic elements measured by dilatation method and X-ray diffraction. *J. Mater. Sci.* **1988**, *23*, 757–760.

(62) Cucka, P.; Barrett, C. S. The crystal structure of Bi and of solid solutions of Pb, Sn, Sb and Te in Bi. *Acta Cryst.* **1962**, *15*, 865–872.

(63) Rettig, S. J.; Trotter, J. Refinement of the structure of orthorhombic sulfur, α-S8. *Acta Cryst.* **1987**, *C43*, 2260–2262.

(64) Razmara, M. F.; Henderson, C. M. B.; Pattrick, R. A. D.; Bell, A. M. T.; Charnock, J. M. The crystal chemistry of the solid solution series between chalcostibite ($CuSbS_2$) and emplectite ($CuBiS_2$). *Mineralogical Magazine* **1997**, *61*, 79–88.

(65) Kyono, A.; Kimata, M. Crystal structures of chalcostibite ($CuSbS_2$) and emplectite ($CuBiS_2$): Structural relationship of stereochemical activity between chalcostibite and emplectite. *American Mineralogist* **2005**, *90*, 162–165.

(66) Malmros, G. The Crystal Structure of α-Bi_2O_3. *Acta Chemica Scandinavica* **1970**, *24*, 384–396.

(67) Evans, H. T. The crystal structures of low chalcocite and djurleite. *Zeitschrift für Kristallographie* **1979**, *150*, 299–320.

(68) Yamamoto, K.; Kashida, S. X-ray study of the average structures of Cu_2Se and $Cu_{1.8}S$ in the room temperature and the high temperature phases. *J. Solid State Chem.* **1991**, *93*, 202–211.

(69) Koto, K.; Morimoto, N. The crystal structure of anilite. *Acta Cryst.* **1970**, *B26*, 915–924.

(70) Evans, H. T.; Konnert, J. A. Crystal structure refinement of covellite. *American Mineralogist* **1976**, *61*, 996–1000.

(71) Hussain, A.; Ahmed, R.; Ali, N.; Shaari, A.; Luo, J.-T.; Fu, Y. Q. Characterization of Cu_3BiS_3 thin films grown by thermally diffusing Cu_2S and Sb_2S_3 layers. *Surface & Coatings Technology* **2017**, *319*, 294–300.

(72) Friedrich, M.; Riefer, A.; Sanna, S.; Schmidt, W. G.; Schindlmayr, A. Phonon dispersion and zero-point renormalization of $LiNbO_3$ from density-functional perturbation theory. *J. Phys.: Condens. Matter* **2015**, *27*, 385402.

(73) Skelton, J. M.; Tiana, D.; Parker, S. C.; Togo, A.; Tanaka, I.; Walsh, A. Influence of the exchange-correlation functional on the quasi-harmonic lattice dynamics of II-VI semiconductors. *J. Chem. Phys.* **2015**, *143*, 064710.

(74) Grigas, J.; Talik, E.; Lazauskas, V. X-Ray Photoelectron Spectra and Electronic Structure of Bi_2S_3 Crystals. *Phys. Stat. Sol. (b)* **202**, *232*, 220–230.

(75) Prabhakar, T.; Jampana, N. Effect of Sodium Diffusion on the Structural and Electrical Properties of Cu_2ZnSnS_4 Thin Films. *Sol. Energy Mater. Sol. Cells* **2011**, *95*, 1001–1004.

(76) Rudmann, D.; Bilger, G.; Kaelin, M.; Haug, F. J.; Zogg, H.; Tiwari, A. N. Structural Properties of Cu(In,Ga)Se_2 Thin Films. *Thin Solid Films* **2003**, *431–432*, 37–40.

(77) Kranz, L.; Perrenoud, J.; Pianezzi, F.; Gretener, C.; Rossbach, P.; Buecheler, S.; Tiwari, A. N. Effect of Sodium on Recrystallization and Photovoltaic Properties of CdTe Solar Cells. *Sol. Energy Mater. Sol. Cells* **2012**, *105*, 213–219.

(78) Lebugle, A.; Axelsson, U.; Nyholm, R.; Mårtensson, N. Experimental L and M Core Level Binding Energies for the Metals 22 Ti to 30 Zn. *Phys. Scr.* **1981**, *23*, 825–827.

(79) Nyholm, R.; Mårtensson, N.; Lebugle, A.; Axelsson, U. Auger and Coster-Kronig Broadening Effects in the 2p and 3p Photoelectron Spectra from the Metals 22 Ti- 30 Zn. *J. Phys. F Met. Phys.* **1981**, *11*, 1727–1733.

(80) Coster, D.; L. Kronig, R. D. New Type of Auger Effect and Its Influence on the X-Ray Spectrum. *Physica* **1935**, *2*, 13–24.

(81) Lenglet, M.; Kartouni, K.; Machefert, J.; Claude, J. M.; Steinmetz, P.; Beauprez, E.; Heinrich, J.; Celati, N. Low Temperature Oxidation of Copper: The Formation of CuO. *Mater. Res. Bull.* **1995**, *30*, 393–403.

(82) Biesinger, M. C.; Lau, L. W. M.; Gerson, A. R.; Smart, R. S. C. Resolving Surface Chemical States in XPS Analysis of First Row Transition Metals, Oxides and Hydroxides: Sc, Ti, V, Cu and Zn. *Appl. Surf. Sci.* **2010**, *257*, 887–898.

(83) Nyholm, R.; Berndtsson, A.; Mårtensson, N. Core Level Binding Energies for the Elements Hf to Bi (Z=72–83). *J. Phys. C Solid State Phys.* **1980**, *13*, L1091–L1096.

(84) Morgan, W. E.; Van Wazer, J. R. Binding Energy Shifts in the X-Ray Photoelectron Spectra of a Series of Related Group IVa Compounds. *J. Phys. Chem.* **1973**, *77*, 964–969.

(85) Debies, T. P.; Rabalais, J. W. X-Ray Photoelectron Spectra and Electronic Structure of Bi_2X_3 (X = O, S, Se, Te). *Chem. Phys.* **1977**, *20*, 277–283.

(86) Dharmadhikari, V. S.; Sainkar, S. R.; Badrinarayan, S.; Goswami, A. Characterisation of Thin Films of Bismuth Oxide by X-Ray Photoelectron Spectroscopy. *J. Electron Spectros. Relat. Phenomena* **1982**, *25*, 181–189.

(87) Schuhl, Y.; Baussart, H.; Delobel, R.; Le Bras, M.; Leroy, J.-M. Study of Mixed-Oxide Catalysts Containing Bismuth, Vanadium and Antimony. *J. Chem. Soc. Faraday Trans I* **1983**, *79*, 2055–2069.

(88) Hutchins, E. B.; Lenher, V. Pentavalent Bismuth. *J. Am. Chem. Soc.* **1907**, *29*, 31–33.

(89) Leontie, L.; Caraman, M.; Alexe, M.; Harnagea, C. Structural and Optical Characteristics of Bismuth Oxide Thin Films. *Surf. Sci.* **2002**, *507–510*, 480–485.

(90) George, J.; Pradeep, B.; Joseph, K. S. Oxidation of Bismuth Films in Air and Superheated Steam. *Thin Solid Films* **1986**, *144*, 255–264.

(91) Shalvoy, R. B.; Fisher, G. B.; Stiles, P. J. Bond Ionicity and Structural Stability of Some Average-Valence-Five Materials Studied by X-Ray Photoemission. *Phys. Rev. B* **1977**, *15*, 1680–1697.

(92) Powell, C. J. Recommended Auger Parameters for 42 Elemental Solids. *J. Electron Spectros. Relat. Phenomena* **2012**, *185*, 1–3.

(93) Barrie, A.; Drummond, I. W.; Herd, Q. C. Correlation of Calculated and Measured 2p Spin-Orbit Splitting by Electron Spectroscopy Using Monochromatic X-Radiation. *J. Electron Spectros. Relat. Phenomena* **1974**, *5*, 217–225.

(94) Peisert, H.; Chassé, T.; Streubel, P.; Meisel, A.; Szargan, R. Relaxation Energies in XPS and XAES of Solid Sulfur Compounds. *J. Electron Spectros. Relat. Phenomena* **1994**, *68*, 321–328.

(95) Smart, R. S. C.; Amarantidis, J.; Skinner, W. M.; Prestidge, C. A.; La Vanier, L.; Grano, S. R. Surface Analytical Studies of Oxidation and Collector Adsorption in Sulfide Mineral Flotation. *Scanning Microscopy* **2003**, *12*, 3–62.

(96) Bär, M.; Schubert, B.-A.; Marsen, B.; Krause, S.; Pookpanratana, S.; Unold, T.; Weinhardt, L.; Heske, C.; Schock, H.-W. Native Oxidation and Cu-Poor Surface Structure of Thin Film Cu_2ZnSnS_4 Solar Cell Absorbers. *Appl. Phys. Lett.* **2011**, *99*, 112103.

(97) Partain, L. D.; Schneider, R. A.; Donaghey, L. F.; McLeod, P. S. Surface Chemistry of Cu_xS and Cu_xS/CdS Determined from X-Ray Photoelectron Spectroscopy. *J. Appl. Phys.* **1985**, *57*, 5056–5065.

(98) Lindberg, B. J.; Hamrin, K.; Johansson, G.; Gelius, U.; Fahlman, A.; Nordling, C.; Siegbahn, K. Molecular Spectroscopy by Means of ESCA II. Sulfur Compounds. Correlation of Electron Binding Energy with Structure. *Phys. Scr.* **1970**, *1*, 286–298.

(99) Chen, D.; Shen, G.; Tang, K.; Liu, X.; Qian, Y.; Zhou, G. The Synthesis of Cu_3BiS_3 Nanorods via a Simple Ethanol-Thermal Route. *J. Cryst. Growth* **2003**, *253*, 512–516.

(100) Yin, J.; Jia, J. Synthesis of Cu_3BiS_3 Nanosheet Films on TiO_2 Nanorod Arrays by a Solvothermal Route and Their Photoelectrochemical Characteristics. *CrystEngComm* **2014**, *16*, 2795.

(101) Gerson, A. R.; Bredow, T. Interpretation of Sulphur 2p XPS Spectra in Sulfide Minerals by Means of Ab Initio Calculations. *Surf. Interface Anal.* **2000**, *29*, 145–150.

(102) Altamura, G.; Vidal, J. Impact of Minor Phases on the Performances of CZTSSe Thin-Film Solar Cells. *Chem. Mater.* **2016**, *28*, 3540–3563.

(103) Meeder, A.; Weinhardt, L.; Stresing, R.; Marron, D. F.; Wurz, R.; Babu, S. M.; Schedel-Niedrig, T.; Lux-Steiner, M. C.; Heske, C.; Umbach, E. Surface and Bulk Properties of $CuGaSe_2$ Thin Films. *J. Phys. Chem. Solids* **2003**, *64*, 1553–1557.

(104) Delbos, S. Këwhile Thin Films for Photovoltaics: A Review. *EPJ Photovoltaics* **2012**, *3*, 35004.

(105) Bär, M.; Schubert, B. A.; Marsen, B.; Wilks, R. G.; Blum, M.; Krause, S.; Pookpanratana, S.; Zhang, Y.; Unold, T.; Yang, W.; Weinhardt, L.; Heske, C.; Schock, H. W. Cu_2ZnSnS_4 Thin-Film Solar Cell Absorbers Illuminated by Soft X-Rays. *J. Mater. Res.* **2012**, *27*, 1097–1104.

(106) Zeng, Y.; Li, H.; Qu, B.; Xiang, B.; Wang, L.; Zhang, Q.; Li, Q.; Wang, T.; Wang, Y. Facile Synthesis of Flower-like Cu3BiS3 Hierarchical Nanostructures and Their Electrochemical Properties for Lithium-Ion Batteries. *CrystEngComm* **2012**, *14*, 550–554.

(107) Ganose, A. M.; Butler, K. T.; Walsh, A.; Scanlon, D. O. Relativistic electronic structure and band alignment of BiSI and BiSeI: candidate photovoltaic materials. *J. Mater. Chem. A* **2016**, *4*, 2060–2068.

(108) Filip, M. R.; Patrick, C. E.; Giustino, F. GW quasiparticle band structures of stibnite, antimonselite, bismuthinite, and guanajuatite. *Phys. Rev. B* **2013**, *87*, 205125.

(109) Lehner, A. J.; Wang, H.; Fabini, D. H.; Liman, C. D.; Hébert, C.-A.; Perry, E. E.; Wang, M.; Bazan, G. C.; Chabinyc, M. L.; Seshadri, R. Electronic structure and photovoltaic application of BiI_3. *Appl. Phys. Lett.* **2015**, *107*, 131109.

(110) Tiwari, D.; Alibhai, D.; Fermin, D. J. Above 600 mV Open-Circuit Voltage BiI_3 Solar Cells. *ACS Energy Lett.* **2018**, *3*, 1882–1886.

(111) Wei, S. H.; Zunger, A. Calculated Natural Band Offsets of All II-VI and III-V Semiconductors: Chemical Trends and the Role of Cation d Orbitals. *Appl. Phys. Lett.* **1998**, *72*, 2011–2013.

(112) Klein, A. Energy Band Alignment in Chalcogenide Thin Film Solar Cells from Photoelectron Spectroscopy. *J. Phys. Condens. Matter* **2015**, *27*, 134201.

(113) Burton, L. A.; Walsh, A. Band Alignment in SnS Thin-Film Solar Cells: Possible Origin of the Low Conversion Efficiency. *Appl. Phys. Lett.* **2013**, *102*, 132111.

(114) Hinuma, Y.; Oba, F.; Kumagai, Y.; Tanaka, I. Ionization Potentials of (112) and (11$\bar{2}$) Facet Surfaces of $CuInSe_2$ and $CuGaSe_2$. *Phys. Rev. B* **2012**, *86*, 245433.

(115) Teeter, G. X-Ray and Ultraviolet Photoelectron Spectroscopy Measurements of Cu-Doped CdTe(111)-B: Observation of Temperature-Reversible Cu_xTe Precipitation and Effect on Ionization Potential. *J. Appl. Phys.* **2007**, *102*, 034504.

(116) Whitcher, T. J.; Yeoh, K. H.; Chua, C. L.; Woon, K. L.; Chanlek, N.; Nakajima, H.; Saisopa, T.; Songsiriritthigul, P. The Effect of Carbon Contamination and Argon Ion Sputtering on the Work Function of Chlorinated Indium Tin Oxide. *Curr. Appl. Phys.* **2014**, *14*, 472–475.

(117) Mesa, F.; Gordillo, G.; Dittrich, T.; Ellmer, K.; Baier, R.; Sadewasser, S. Transient Surface Photovoltage of P-Type Cu_3BiS_3. *Appl. Phys. Lett.* **2010**, *96*, 82113.

(118) Kim, J.; Lägel, B.; Moons, E.; Johansson, N. Kelvin Probe and Ultraviolet Photoemission Measurements of Indium Tin Oxide Work Function: A Comparison. *Synth. Met.* **2000**, *111*, 311–314.

(119) Pookpanratana, S.; Repins, I.; Bär, M.; Weinhardt, L.; Zhang, Y.; Felix, R.; Blum, M.; Yang, W.; Heske, C.; Bar, M.; Felix, R. CdS/Cu(In,Ga)Se_2 Interface Formation in High-Efficiency Thin Film Solar Cells. *Appl. Phys. Lett.* **2010**, *97*, 074101.

(120) Kumar, S. G.; Rao, K. S. R. K. Physics and Chemistry of CdTe/CdS Thin Film Heterojunction Photovoltaic Devices: Fundamental and Critical Aspects. *Energy Environ. Sci.* **2014**, *7*, 45–102.

(121) Minemoto, T.; Matsui, T.; Takakura, H.; Y., H.; Negami, T.; Hashimoto, Y.; Uenoyama, T.; Kitagawa, M. Theoretical Analysis of the Effect of Conduction Band

Offset of window/CIS Layers on Performance of CIS Solar Cells Using Device Simulation. *Sol. Energy Mater. Sol. Cells* **2001**, *67*, 83–88.

(122) Sugiyama, M.; Shimizu, T.; Kawade, D.; Ramya, K.; Ramakrishna Reddy, K. T. Experimental Determination of Vacuum-Level Band Alignments of SnS-Based Solar Cells by Photoelectron Yield Spectroscopy. *J. Appl. Phys.* **2014**, *115*, 083508.

(123) Sinsermsuksakul, P.; Hartman, K.; Bok Kim, S.; Heo, J.; Sun, L.; Hejin Park, H.; Chakraborty, R.; Buonassisi, T.; Gordon, R. G. Enhancing the Efficiency of SnS Solar Cells via Band-Offset Engineering with a Zinc Oxysulfide Buffer Layer. *Appl. Phys. Lett.* **2013**, *102*, 053901.

(124) Sinsermsuksakul, P.; Sun, L.; Lee, S. W.; Park, H. H.; Kim, S. B.; Yang, C.; Gordon, R. G. Overcoming Efficiency Limitations of SnS-Based Solar Cells. *Adv. Energy Mater.* **2014**, *4*, 1400496.

(125) Durose, K.; Asher, S. E.; Jaegermann, W.; Levi, D.; McCandless, B. E.; Metzger, W.; Moutinho, H.; Paulson, P. D.; Perkins, C. L.; Sites, J. R.; Teeter, G.; Terheggen, M. Physical Characterization of Thin-Film Solar Cells. *Prog. Photovoltaics* **2004**, *12*, 177–217.

(126) Morasch, J.; Li, S.; Brötz, J.; Jaegermann, W.; Klein, A. Reactively Magnetron Sputtered Bi_2O_3 Thin Films: Analysis of Structure, Optoelectronic, Interface, and Photovoltaic Properties. *Phys. status solidi (a)* **2014**, *211*, 93–100.

(127) Shuk, P. Oxide Ion Conducting Solid Electrolytes Based on Bi_2O_3. *Solid State Ionics* **1996**, *89*, 179–196.

(128) Xu, Y.; Schoonen, M. A. A. The Absolute Energy Positions of Conduction and Valence Bands of Selected Semiconducting Minerals. *Am. Mineral.* **2000**, *85*, 543–556.

(129) Ley, L.; Pollak, R. A.; McFeely, F. R.; Kowalczyk, S. P.; Shirley, D. A. Total Valence-Band Densities of States of III-V and II-VI Compounds from X-Ray Photoemission Spectroscopy. *Phys. Rev. B* **9**, *1974*, 600–621.

(130) Fadley, C. S.; Shirley, D. A. Electronic Densities of States from X-Ray Photoelectron Spectroscopy. *J. Res. Nat. Bur. Stand. (Phys. Chem.)* **1970**, *74A*, 543–558.

(131) Mann, J. B.; Meek, T. L.; Allen, L. C. Configuration Energies of the Main Group Elements. *J. Am. Chem. Soc.* **2000**, *122*, 2780–2783.

(132) Mann, J. B.; Meek, T. L.; Knight, E. T.; Capitani, J. F.; Allen, L. C. Configuration Energies of the D-Block Elements. *J. Am. Chem. Soc.* **2000**, *122*, 5132–5137.

(133) Maeda, T.; Wada, T. Characteristics of Chemical Bond and Vacancy Formation in Chalcopyrite-Type $CuInSe_2$ and Related Compounds. *phys. status solidi (c)* **2009**, *6*, 1312–1316.

(134) Zhang, Y.; Yuan, X.; Sun, X.; Shih, B.-C.; Zhang, P.; Zhang, W. Comparative Study of Structural and Electronic Properties of Cu-Based Multinary Semiconductors. *Phys. Rev. B* **2011**, *84*, 075127.

(135) Lukashev, P.; Lambrecht, W. R. L.; Kotani, T.; van Schilfgaarde, M. Electronic and Crystal Structure of Cu_2S: Full-Potential Electronic Structure Calculations. *Phys. Rev. B* **2007**, *76*, 195202.

(136) Walsh, A.; Payne, D. J.; Egdell, R. G.; Watson, G. W. Stereochemistry of Post-Transition Metal Oxides: Revision of the Classical Lone Pair Model. *Chem. Soc. Rev.* **2011**, *40*, 4455–4463.

(137) Yu, L.; Kokenyesi, R. S.; Keszler, D. A.; Zunger, A. Inverse Design of High Absorption Thin-Film Photovoltaic Materials. *Adv. Energy Mater.* **2013**, *3*, 43–48.

(138) Menéndez-Proupin, E.; Gutiérrez, G.; Palmero, E.; Peña, J. L. Electronic Structure of Crystalline Binary and Ternary CdTeO Compounds. *Phys. Rev. B* **2004**, *70*, 035112.

(139) Meijer, P. H. E.; Pecheur, P.; Toussaint, G. Electronic Structure of the Cd Vacancy in CdTe. *phys. status solidi* **1987**, *140*, 155–162.

(140) Yang, B.; Wang, L.; Han, J.; Zhou, Y.; Song, H.; Chen, S.; Zhong, J.; Lv, L.; Niu, D.; Tang, J. $CuSbS_2$ as a Promising Earth-Abundant Photovoltaic Absorber Material: A Combined Theoretical and Experimental Study. *Chem. Mater.* **2014**, *26*, 3135–3143.

(141) Chen, S.; Yang, J.-H.; Gong, X. G.; Walsh, A.; Wei, S.-H. Intrinsic Point Defects and Complexes in the Quaternary Kesterite Semiconductor Cu_2ZnSnS_4. *Phys. Rev. B* **2010**, *81*, 245204.

(142) Siebentritt, S.; Igalson, M.; Persson, C.; Lany, S. The Electronic Structure of Chalcopyrites-Bands, Point Defects and Grain Boundaries. *Prog. Photovoltaics Res. Appl.* **2010**, *18*, 390–410.

(143) Klein, A. Energy Band Alignment at Interfaces of Semiconducting Oxides: A Review of Experimental Determination Using Photoelectron Spectroscopy and Comparison with Theoretical Predictions by the Electron Affinity Rule, Charge Neutrality Levels, and the Common Anion. *Thin Solid Films* **2012**, *520*, 3721–3728.

(144) Zakutayev, A.; Caskey, C. M.; Fioretti, A. N.; Ginley, D. S.; Vidal, J.; Stevanovic, V.; Tea, E.; Lany, S. Defect Tolerant Semiconductors for Solar Energy Conversion. *J. Phys. Chem. Lett.* **2014**, *5*, 1117–1125.

(145) Sullivan, I.; Zoellner, B.; Maggard, P. A. Copper(I)-Based p-Type Oxides for Photoelectrochemical and Photovoltaic Solar Energy Conversion. *Chem. Mater.* **2016**, *28*, 5999–6016.

(146) Chen, S.; Gong, X. G.; Walsh, A.; Wei, S.-H. Crystal and Electronic Band Structure of Cu_2ZnSnX_4 (X=S and Se) Photovoltaic Absorbers: First-Principles Insights. *Appl. Phys. Lett.* **2009**, *94*, 041903.

(147) King, P. D. C.; Veal, T. D.; Jefferson, P. H.; Hatfield, S. A.; Piper, L. F. J.; McConville, C. F.; Fuchs, F.; Furthmüller, J.; Bechstedt, F.; Lu, H.; Schaff, W. J. Determination of the Branch-Point Energy of InN: Chemical Trends in Common-Cation and Common-Anion Semiconductors. *Phys. Rev. B* **2008**, *77*, 045316.

(148) Li, Y.-H.; Walsh, A.; Chen, S.; Yin, W.-J.; Yang, J.-H.; Li, J.; Da Silva, J. L. F.; Gong, X. G.; Wei, S.-H. Revised Ab Initio Natural Band Offsets of All Group IV, II-VI, and III-V Semiconductors. *Appl. Phys. Lett.* **2009**, *94*, 212109.

For Table of Contents Only

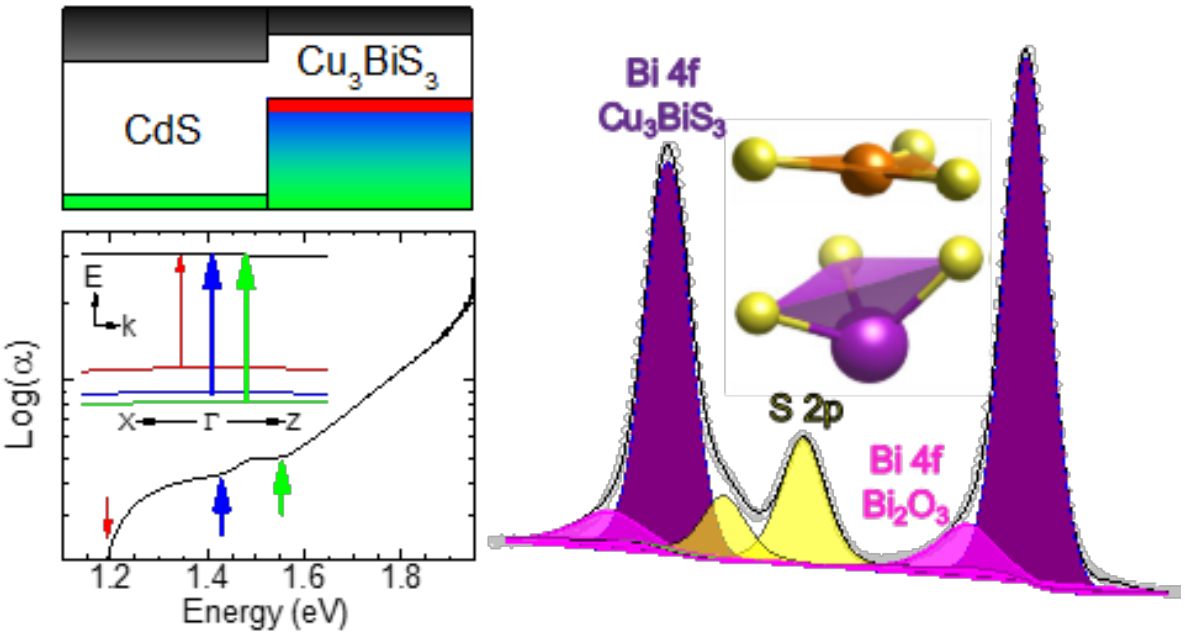

Figure 14